

# Satellite Autonomous Clock Fault Monitoring with Inter-Satellite Ranges Using Euclidean Distance Matrices

2025 May 20 [2021]

Keigai Iiyama | Daniel Neamati | Grace Gao

<sup>1</sup>Department of Aeronautics and Astronautics,  
Stanford University, California, United States

## Correspondence

Grace Gao, Department of Aeronautics and Astronautics, Stanford University, California, United States  
Email: gracegao@stanford.edu

## Abstract

To address the need for robust positioning, navigation, and timing services in lunar environments, this paper proposes a novel onboard clock phase jump detection framework for satellite constellations using range measurements obtained from dual one-way inter-satellite links. Our approach leverages vertex redundantly rigid graphs to detect faults without relying on prior knowledge of satellite positions or clock biases, providing flexibility for lunar satellite networks with diverse satellite types and operators. We model satellite constellations as graphs, where satellites are vertices and inter-satellite links are edges. The proposed algorithm detects and identifies satellites with clock jumps by monitoring the singular values of the geometric-centered Euclidean distance matrix (GCEDM) of 5-clique sub-graphs. The proposed method is validated through simulations of a GPS constellation and a notional constellation around the Moon, demonstrating its effectiveness in various configurations.

## Keywords

lunar positioning, navigation, and timing (PNT), satellite constellation, fault detection, inter-satellite links

## 1 | INTRODUCTION

To meet the growing need for robust positioning, navigation, and timing (PNT) services at the lunar surface and lunar orbits, NASA and its international partners are collaborating to develop LunaNet (Israel et al., 2020), a network of networks providing data relay, PNT, detection, and science services. In LunaNet, these services are provided through cooperation among interoperable systems that evolve over time to meet the growing needs for these services, efficiently establishing a reliable, sustainable, and scalable network.

It is crucial to monitor LunaNet navigation satellites for the reliable operation of safety-critical missions, such as lunar landing and human missions on the lunar surface. The quality of lunar navigation signals can be compromised by various system faults, such as clock runoffs (e.g., phase and frequency jumps (Weiss et al., 2010)), unflagged maneuvers, failures in satellite payload signal generation components, and code-carrier incoherence (Walter et al., 2018). While the LunaNet Relay Service Documents (SRD) state that robustness of the navigation signal should be a key consideration for LunaNet (National Aeronautics and Space Administration, 2022), The specific methodology to monitor faults on LunaNet satellites has not yet been solidified.

The currently implemented integrity monitoring method for terrestrial GNSS can be categorized into three methods: (1) ground-based monitoring, (2) receiver autonomous integrity monitoring (RAIM), and (3) satellite-based integrity monitoring (SAIM). The first method relies on a network of ground-based monitoring stations at known positions to track and collect the GNSS signals, which are then collected and processed at a central computing center to compute corrections and integrity information (Misra et al., 1993). The system fault alerts are provided as integrity information from GNSS augmentation systems, such as the satellite-based augmentation system (SBAS) (Van Diggelen, 2009). The second method, RAIM, uses redundant measurements from GNSS satellites to detect and exclude faulty satellites on the receiver side (Misra et al., 1993). The third method, SAIM,

computes the integrity information onboard the navigation satellite to detect satellite-related faults such as clock anomalies and ephemeris errors (Xu et al., 2011).

While the first two methods are well established and widely adopted for integrity monitoring of terrestrial GNSS, their adoption may be more limited for lunar constellations. The first method requires a network of ground-based monitoring stations, which would be expensive and impractical to deploy widely on the lunar surface, especially for near-term constellations. The second method, RAIM, requires at least five satellites in view to detect (six satellites in view to exclude) a faulty satellite, which limits its availability in lunar constellations with a smaller number of navigation satellites than terrestrial GNSS.

The third method, SAIM, has several advantages compared with the other two methods: (1) faster time to alert enabled by eliminating the latency associated with data collection, processing, and uplink on the ground (2) the use of precise inter-satellite range (ISR) measurements (BeiDou satellites have demonstrated 10 cm accuracy (Zhang et al., 2024)) that are unaffected by the ionosphere and troposphere, and (3) the monitoring can be operated autonomously within the constellation and independently of ground monitoring. The autonomous nature of SAIM is particularly valuable for early lunar deployments, when lunar surface stations will be scarce or absent.

SAIM has been implemented in the BeiDou GNSS system to detect clock phase and frequency jumps by comparing the outputs of multiple onboard clocks ( ), at the cost of adding extra hardware. Several other works have also proposed SAIM methods utilizing ISR measurements, which detect ephemeris anomalies by directly comparing the ISR measurement and the predicted range from the ephemeris ( ).

However, existing SAIM schemes process ISR measurements on a per-satellite basis, making their minimal detectable bias (MDB) dependent on ephemeris accuracy (Xu et al., 2011). This dependence may prove challenging for lunar constellations, where orbit determination and time synchronization are more difficult than for terrestrial GNSS. One remedy is to aggregate all ISR measurements centrally, form a linear system of residual equations, and apply data-snooping techniques ( ) to isolate faulty satellites. Yet this approach still requires the satellite positions to compute the residuals, which may not be (easily) available onboard all LunaNet nodes, since the interoperable LunaNet network may include links to satellites dedicated to communication or science tasks rather than PNT (Giordano et al., 2023).

In this paper, we propose a new algorithm to detect phase jumps in the satellite clocks that uses dual one-way ISR measurements. The proposed method operates directly on the observed ISRs and not the residuals, and thus does not require prior information or computation of the position or clock biases of the satellites. It detects faults by identifying biases injected into ISR measurements whenever a satellite's onboard clock experiences a phase jump between two dual one-way links. We prove that we are able to detect fault satellites (satellites with clocks that experienced phase jumps) by assessing the realizability of the 5-clique (a fully connected graph of 5 nodes) subgraphs, since these subgraphs remain rigid (graphs that cannot be susceptible to continuous flexing are called rigid graphs), after removing any vertex from the graph (Alireza Motevallian et al., 2015). The concept of the algorithm is illustrated in Figure 1.

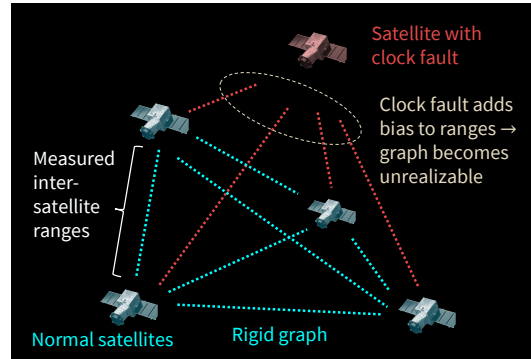


Figure 1 Concept of the proposed fault detection algorithm

Our proposed method monitors the singular values of the geometric-centered Euclidean distance matrix (GCEDM) (Dokmanić et al., 2015) constructed from the ISR measurements, to check if 5-clique subgraphs are realizable in 3-dimensional space. In

particular, we provide analytical expressions of the distribution of the squared 4th singular value under the presence of noise and biases in the range measurement, and design hypothesis tests to detect and identify the satellite clock with phase jumps.

The contribution of this paper is summarized below. This work is based on our prior conference paper presented at the 2024 ION GNSS+ Conference (Iiyama, Neamati, & Gao, 2024), but includes key theoretical and simulation updates beyond our prior publication.

- We establish the necessary graph topology—specifically, vertex redundant rigidity—for unambiguous fault detection from ISR measurements.
- We prove key rank properties of EDMs and GCEDMs, and derive the distribution of the squared 4th singular value under noise and bias.
- We develop a hypothesis test based on the GCEDM's 4th singular value to detect and identify satellite clock phase jumps.
- We validate our approach via simulations of a GPS constellation and a notional lunar constellation, analyzing the impact of hyperparameters and fault magnitudes, and comparing fault detection and false alarm rates against residual-based baseline methods.

Note that our method is not intended to completely replace decades of research in the existing fault detection methods. Rather, our method provides new theoretical and practical insights to view the fault detection problem from a different perspective.

The paper is arranged as follows. Section 2 introduces the formulation of the dual one-way ISR measurements. Section 3 describes two baseline clock jump detection methods, which use ISR measurement residuals computed from the ephemeris. Section 4 describes the proposed fault detection algorithm based on singular values of the GCEDM. Section 5 provides simulation results for the GPS constellation and a notional lunar constellation. The paper concludes with section 6.

## 2 | MEASUREMENTS FROM INTER-SATELLITE LINKS

### 2.1 | Dual One-Way Inter-satellite Range Measurement

We consider two satellites establishing a dual one-way inter-satellite link (ISL) as shown in Figure 2 to obtain ISR measurements. In this section, we formulate the ISR measurement model for the dual one-way link, based on Zhang et al. (2024).

Let  $i, j$  be the indices of the two satellites establishing the link, and  $\mathbf{x}_i, \mathbf{x}_j \in \mathbb{R}^3$  the position vector of the two satellites. The two observation equations for the dual one-way link can be expressed as follows:

$$\rho_{ij}(t_1) = \|\mathbf{x}_j(t_1) - \mathbf{x}_i(t_1 - \Delta t_1)\| + c \cdot [\tau_j(t_1) - \tau_i(t_1 - \Delta t_1)] + c \cdot [\Delta t_j^{rx} + \Delta t_i^{tx}] + \omega_1 \quad (1)$$

$$\rho_{ji}(t_2) = \|\mathbf{x}_i(t_2) - \mathbf{x}_j(t_2 - \Delta t_2)\| + c \cdot [\tau_i(t_2) - \tau_j(t_2 - \Delta t_2)] + c \cdot [\Delta t_i^{rx} + \Delta t_j^{tx}] + \omega_2 \quad (2)$$

where  $\rho_{ij}, \rho_{ji}$  represents the measured pseudoranges for the two links where satellite  $i$  and  $j$  receives the signal at  $t_1$  and  $t_2$ , respectively.  $\Delta t_1$  and  $\Delta t_2$  are the signal travel times;  $\tau_i$  and  $\tau_j$  are the clock offsets;  $t^{rx}$  and  $t^{tx}$  represent hardware delays of the receiving channel and the transmitting channels;  $\omega_1$  and  $\omega_2$  are the measurement noises. We assume the phase center offset and relativistic effects are corrected, and not included in the equations.

To eliminate the common errors between the two links, the two measurements are transformed into the common time  $t_0$  using the following equations:

$$\rho_{ij}(t_0) = \rho_{ij}(t_1) + \Delta\rho_{ij} = \|\mathbf{x}_j(t_0) - \mathbf{x}_i(t_0)\| + c \cdot [\tau_j(t_0) - \tau_i(t_0)] + c \cdot [\Delta t_j^{rx} + \Delta t_i^{tx}] + \omega_{1,0} \quad (3)$$

$$\rho_{ji}(t_0) = \rho_{ji}(t_2) + \Delta\rho_{ji} = \|\mathbf{x}_i(t_0) - \mathbf{x}_j(t_0)\| + c \cdot [\tau_i(t_0) - \tau_j(t_0)] + c \cdot [\Delta t_i^{rx} + \Delta t_j^{tx}] + \omega_{2,0} \quad (4)$$

where  $\Delta\rho_{ij}$  and  $\Delta\rho_{ji}$  are the corrections of satellite position and clocks that can be expressed as:

$$\Delta\rho_{ij} = \|\mathbf{x}_j(t_0) - \mathbf{x}_i(t_0)\| - \|\mathbf{x}_j(t_1) - \mathbf{x}_i(t_1 - \Delta t_1)\| + c \cdot [\tau_j(t_0) - \tau_i(t_0) - \tau_j(t_1) + \tau_i(t_1 - \Delta t_1)] \quad (5)$$

$$\Delta\rho_{ji} = \|\mathbf{x}_i(t_0) - \mathbf{x}_j(t_0)\| - \|\mathbf{x}_i(t_2) - \mathbf{x}_j(t_2 - \Delta t_2)\| + c \cdot [\tau_i(t_0) - \tau_j(t_0) - \tau_i(t_1) + \tau_j(t_1 - \Delta t_1)] \quad (6)$$

The corrections  $\Delta\rho_{ij}$  and  $\Delta\rho_{ji}$  are obtained using the predicted satellite ephemeris. Therefore, the accuracy of the corrections depends on the accuracy of the satellite velocity and the satellite clock drift of the ephemeris. For Beidou satellites, the accuracy of the predicted satellite velocity and clock drift is better than 0.1 mm/s and  $1 \times 10^{-13}$  s/s, resulting in  $\Delta\rho_{ij}, \Delta\rho_{ji} < 1.0$  cm

when  $t_2 - t_1 < 3$  s (Xie et al., 2022). For LunaNet satellites, the specification for the sum of velocity and clock drift error (converted to velocity by multiplying with lightspeed) in the ephemeris is 1.2 mm/s (for  $3\sigma$ ), so the error of the correction terms can be in order of centimeters (National Aeronautics and Space Administration, 2022). Whenever further accuracy is required or velocity ephemeris information is not available, we can also utilize the inter-satellite range rate measurements between the satellites for correction (Iiyama, Vila, & Gao, 2024).

The sum and differences of equations (5) and (6) can be expressed as

$$r_{ij}(t_0) = \frac{\rho_{ij}(t_0) + \rho_{ji}(t_0)}{2} = \|\mathbf{x}_j(t_0) - \mathbf{x}_i(t_0)\| + \bar{b}_{ij}^{range} + \frac{\omega_{1,0} + \omega_{2,0}}{2} \quad (7)$$

$$\tau_{ij}(t_0) = \frac{\rho_{ij}(t_0) - \rho_{ji}(t_0)}{2} = c \cdot [\tau_j(t_0) - \tau_i(t_0)] + \bar{b}_{ij}^{clock} + \frac{\omega_{1,0} - \omega_{2,0}}{2} \quad (8)$$

where  $r_{ij}(t_0)$  and  $\tau_{ij}(t_0)$  are the clock-free and geometry-free observations.  $b_{ij}$  and  $b_{ji}$  are the bias terms due to hardware delays as follows

$$\bar{b}_{ij}^{range} = c \cdot \frac{\Delta t_j^{rx} + \Delta t_i^{tx} + \Delta t_i^{rx} + \Delta t_j^{tx}}{2} \quad (9)$$

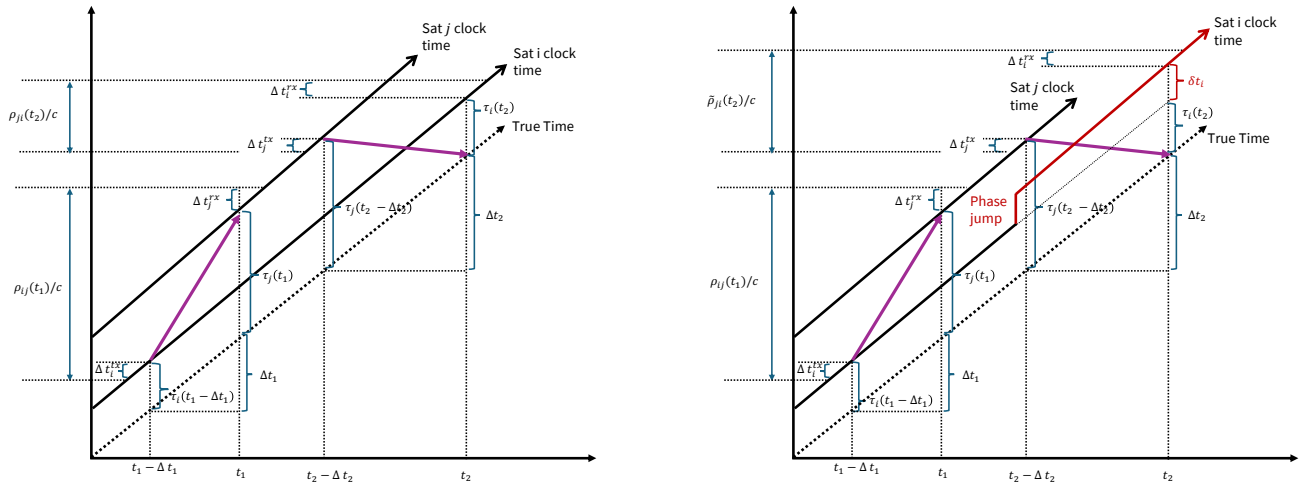
$$\bar{b}_{ij}^{clock} = c \cdot \frac{\Delta t_j^{rx} + \Delta t_i^{tx} - \Delta t_i^{rx} - \Delta t_j^{tx}}{2} \quad (10)$$

The bias terms  $b_{ij}^{range}$  and  $b_{ij}^{clock}$  are usually constant over a short term and can therefore be estimated using filtering techniques. In this paper, we assume that these biases can be estimated within certain errors, and the error terms are included in the measurement noises, resulting in the following two equations.

$$r_{ij}(t_0) = \|\mathbf{x}_i - \mathbf{x}_j\| + \omega_{range} \quad \text{clock-free combination} \quad (11)$$

$$\tau_{ij}(t_0) = c [\tau_j(t_0) - \tau_i(t_0)] + \omega_{clock} \quad \text{geometry-free combination} \quad (12)$$

For ISLs in Beidou, the observed  $\omega_{range}$  and  $\omega_{clock}$  can be approximated as a Gaussian distribution with standard deviations in the order of centimeters.



(a) Dual one-way link between the two satellites, when there is no phase jump at either satellite. Two pseudorange measurements  $\rho_{ij}(t_1)$  and  $\rho_{ji}(t_2)$  are obtained.

(b) Dual one-way link between the two satellites when there is a phase jump at satellite *i*. When the phase jump occurs at  $t_1 - \Delta t_1 < t < t_2$ , a bias  $c\delta t_i$  is added to the pseudorange measurement  $\rho_{ji}(t_2)$ .

Figure 2 Dual one-way inter-satellite link measurement between two satellites. Satellite *i* transmits the signal to satellite *j*, received at  $t_1$ , and satellite *j* transmits the signal to satellite *i*, received at  $t_2$ .

## 2.2 | Satellite Clock Phase Jumps

Atomic clocks on navigation satellites occasionally experience a sudden jump in the clock phase. When satellite  $i$ 's clock experiences a phase jump of  $\delta t_i$  (delay) between  $t_1 - \Delta t_1$  and  $t_2$ , as illustrated in Figure 2(b), the corrupted pseudorange measurement  $\tilde{\rho}_{ji}(t_2)$  can be re-written as follows

$$\begin{aligned}\tilde{\rho}_{ji}(t_2) &= \|\mathbf{x}_i(t_2) - \mathbf{x}_j(t_2 - \Delta t_2)\| + c \cdot [\tau_i(t_2) - \tau_j(t_2 - \Delta t_2)] + c \cdot [\Delta t_i^{rx} + \Delta t_j^{tx}] + c \cdot \delta t_i + \omega_2 \\ &= \rho_{ji}(t_2) + c \cdot \delta t_i\end{aligned}\quad (13)$$

The (estimated) correction term will be

$$\begin{aligned}\Delta\tilde{\rho}_{ji} &= \|\mathbf{x}_i(t_0) - \mathbf{x}_j(t_0)\| - \|\mathbf{x}_i(t_2 + \delta t_i) - \mathbf{x}_j(t_2 + \delta t_i - \Delta t_2)\| + c \cdot [\tau_i(t_0) - \tau_j(t_0) - \tau_i(t_1) + \tau_j(t_2 + \delta t_i - \Delta t_2)] \\ &= \Delta\rho_{ij} + \delta\Delta\rho_{ji}\end{aligned}\quad (14)$$

where  $\delta\Delta\rho_{ji}$  is the error in the correction term due to the error in the time stamping of the reception time  $t_2$  to  $t_2 + \delta t_i$ , which can be represented as follows

$$\begin{aligned}\delta\Delta\rho_{ji} &= (\|\mathbf{x}_i(t_2) - \mathbf{x}_j(t_2 - \Delta t_2)\| - \|\mathbf{x}_i(t_2 + \delta t_i) - \mathbf{x}_j(t_2 + \delta t_i - \Delta t_2)\|) + c \cdot [\tau_j(t_2 + \delta t_i - \Delta t_2) - \tau_j(t_2 - \Delta t_2)] \\ &\approx [-\dot{\rho}_{ji}(t_2) + c \cdot \dot{\tau}_j(t_2 - \Delta t_2)] \delta t_i\end{aligned}\quad (15)$$

where  $\dot{\rho}_{ji}$  represents the range-rate of the link between  $j$  and  $i$ , and  $\dot{\tau}_j$  represents the clock drift of the onboard clock at satellite  $j$ . Therefore, the corrected pseudorange at  $t_0$  is

$$\begin{aligned}\tilde{\rho}_{ji}(t_0) &= \tilde{\rho}_{ji}(t_2) + \Delta\tilde{\rho}_{ji} = (\rho_{ji}(t_2) + c\delta t_i) + (\Delta\rho_{ij} + \delta\Delta\rho_{ji}) \\ &\approx (\rho_{ij}(t_2) + \Delta\rho_{ij}) + \delta t_i \cdot [c - \dot{\rho}_{ji}(t_2) + c\dot{\tau}_j(t_2 - \Delta t_2)] \\ &\approx \rho_{ij}(t_0) + c \cdot \delta t_i \quad (\because \dot{\rho}_{ji} \ll c, \dot{\tau}_j \ll 1)\end{aligned}\quad (16)$$

Similary, when satellite  $j$ 's clock experiences a phase jump of  $\delta t_j$  (delay) between  $t_1$  and  $t_2 - \Delta t_2$ , the  $\rho_{ji}$  can be re-written as

$$\tilde{\rho}_{ji}(t_0) \approx \rho_{ij}(t_0) - c \cdot \delta t_j \quad (17)$$

Therefore, the clock-free and geometry combination considering satellite clock jumps is:

$$r_{ij}(t_0) = \|\mathbf{x}_i(t_0) - \mathbf{x}_j(t_0)\| + f_i - f_j + \omega_{range} \quad \text{clock-free combination} \quad (18)$$

$$\tau_{ij}(t_0) = c[\tau_j(t_0) - \tau_i(t_0)] + f_i + f_j + \omega_{clock} \quad \text{geometry-free combination} \quad (19)$$

$$f_i = \begin{cases} \frac{c}{2} \cdot \delta t_i & \text{clock jump } \delta t_i \text{ occurs at satellite } i \text{ for } t \text{ within } t_1 - \Delta t < t < t_2 \\ 0 & \text{satellite } i \text{ 's clock is normal} \end{cases} \quad (20)$$

$$f_j = \begin{cases} \frac{c}{2} \cdot \delta t_j & \text{clock jump } \delta t_j \text{ occurs at satellite } j \text{ for } t \text{ within } t_1 < t < t_2 - \Delta t \\ 0 & \text{satellite } j \text{ 's clock is normal} \end{cases} \quad (21)$$

Note that if the phase jump  $\delta t_i$  occurs at  $t < t_1 - \Delta t_1$  or  $t > t_2$ , and  $\delta t_j$  occurs at  $t < t_1$  or  $t > t_2 - \Delta t_2$ , the errors cancel when  $\tilde{\rho}_{ij}(t_0)$  and  $\tilde{\rho}_{ji}(t_0)$  are added or subtracted. Consequently, these errors do not appear in  $r_{ij}(t_0)$  or  $\tau_{ij}(t_0)$ . Therefore, to improve the likelihood of detecting clock jumps, we should either increase the frequency of the ISL measurements or extend the interval between  $t_1$  and  $t_2$ . However, note that increasing the interval  $t_2 - t_1$  will lead to larger correction errors ( $\Delta\rho_{ij}$  and  $\Delta\rho_{ji}$ ), which in turn results in greater  $\omega_{range}$  and  $\omega_{clock}$ .

## 3 | BASELINE METHODS: CLOCK FAULT DETECTION USING INTER-SATELLITE RANGE RESIDUALS

In this section, we introduce two baseline methods for detecting clock jump faults. The two methods uses the range residuals, which are computed from the ISL range measurements and the ephemeris information.

### 3.1 | Fault Detection Using the Sum of Residuals

The first method is based on the ephemeris fault detection method proposed by Rodríguez-Pérez et al. (2011) and Xu et al. (2011). While the original method was proposed for ephemeris fault detection, it could also be used for clock phase jump detection.

Let  $g_{ij}$  be the range residual of the  $i$ th ISL at time  $t_0$ , which is defined as

$$\begin{aligned} g_{ij} &= r_{ij}(t_0) - \|\hat{\mathbf{x}}_i(t_0) - \hat{\mathbf{x}}_j(t_0)\| \\ &= \|\mathbf{x}_i(t_0) - \mathbf{x}_j(t_0)\| - \|\hat{\mathbf{x}}_i(t_0) - \hat{\mathbf{x}}_j(t_0)\| + f_i - f_j + \omega_{range} \end{aligned} \quad (22)$$

where  $\hat{\mathbf{x}}_i(t_0)$  is the estimated position (from ephemeris) of the  $i$ th satellite at time  $t_0$ ,

The test statistics for the  $i$ th satellite are defined as

$$T_i = \sum_{j=1}^{l_i} \left( \frac{g_{i,j}^2}{\sqrt{2\sigma_r^2 + \sigma_m^2}} \right)^2 \quad (23)$$

where  $l_i$  is the number of ISLs that involve the  $i$ th satellite, and  $\sigma_r^2$  and  $\sigma_m^2$  are the variances of the position estimates in the ephemeris and the variance of ISL range measurement noise ( $\omega_{range}$ ), respectively.

We define the null hypothesis  $\mathcal{H}_{0,i}$  as the absence of faults in the  $i$ th satellite, and the alternative hypothesis  $\mathcal{H}_{a,i}$  as the presence of a fault in the  $i$ th satellite. The test statistic  $T_i$  is distributed as a Chi-squared distribution with  $l_i$  degrees of freedom under the null hypothesis  $\mathcal{H}_0$ . The critical value for the test  $\chi_{\alpha}^2(l_i, 0)$  for the false alarm rate  $\alpha$  is given as

$$\chi_{\alpha}^2(1, 0) = P[\chi^2(1, 0) \leq \chi_{\alpha}^2(1, 0)] = \alpha \quad (24)$$

where  $\chi^2(r, \lambda)$  is the non-central Chi-squared distribution with  $r$  degrees of freedom and the non-centrality parameter  $\lambda$ . The testing procedure is (Xu et al., 2011)

$$\text{Accept } \mathcal{H}_0 \text{ if } \max_{j \in \{1, \dots, n\}} T_j < \sqrt{\chi_{\alpha}^2(1, 0)} \quad (25)$$

otherwise

$$\text{Accept } \mathcal{H}_k \text{ where } k = \operatorname{argmax}_{j \in \{1, \dots, n\}} \frac{T_j}{\sqrt{l_j}} \quad (26)$$

The minimum detectable bias for  $\mathcal{H}_k$  is computed as

$$MDB(k) = \sqrt{\lambda(\alpha, \gamma, 1) \cdot (2\sigma_r^2 + \sigma_m^2)} \quad (27)$$

where the non-centrality parameter  $\lambda(\alpha, \gamma, 1)$  is computed as a function of false alarm rate  $\alpha$  and detection power  $\gamma$  (equal to the miss-detection rate of  $1 - \gamma$ ), by solving for the following equation

$$P_{MD} = P[\chi^2(1, \lambda) \leq \chi_{\alpha}^2(1, 0)] = 1 - \gamma \quad (28)$$

Due to the correlation between  $g_{i,j}$  and  $g_{i,k}$  ( $i \neq k$ ) via the common ephemeris error, the distribution of the test statistic under both hypotheses will not exactly follow a Chi-squared and non-central Chi-squared distribution, respectively. Based on this observation, Xu et al. (2011) proposed to compute a conservative threshold for the test statistic via numerical simulation by using the correlation between two links  $g_{i,j}$  and  $g_{i,k}$  as follows

$$\rho(g_{i,j}, g_{i,k}) \leq \frac{\sigma_r^2}{2\sigma_r^2 + \sigma_m^2} \quad (29)$$

In this paper, we used Imhof's method (Imhof, 1961) to compute the critical value for the test statistic. The detailed procedure is explained in Appendix A.

The advantage of this "sum of residuals" approach is that the fault detection is fully distributed among the satellites. The test is also able to detect the faults in the ephemeris information if they are present. However, the disadvantage of the fault detection method is that the minimum detectable bias is dependent on the ephemeris error  $\sigma_r$ , as shown in Equation (27).

### 3.2 | Data Snooping with Baarda's w-test Statistic

The test in Section 3.1 does not use all the ISL measurements available in the constellation. By testing the null hypothesis on a complete set of measurements from all ISLs, we can lower the minimum detectable bias when the measurement errors are smaller than the ephemeris errors.

Let  $n$  be the number of satellites in the constellation,  $\mathbf{X} \in \mathbb{R}^{3n}$  be the flattened vector of spacecraft positions at time  $t_0$ ,  $\mathbf{Y} \in \mathbb{R}^m$  be the vector of  $m$  inter-satellite range measurements at time  $t_0$ . We also define  $b$  as the bias in the range measurement (equal to  $c\delta t/2$  in Equations (20) and (21)) from one faulty satellite  $f$  which experienced a clock phase jump  $\delta t$ .

The mapping between  $\mathbf{X}$  and  $\mathbf{Y}$  can be represented as the following nonlinear function  $h$ :

$$\mathbf{Y} = h(\mathbf{X}) + \mathbf{c}_f b + \omega, \quad \omega \sim \mathcal{N}(\mathbf{0}_m, \Sigma_{yy}) \quad (30)$$

where  $\Sigma_{yy} = \sigma_m^2 \mathbf{I}_m$  is the covariance of the range measurements, and  $\mathbf{c}_f$  is a known vector which maps the fault satellites to the corrupted range measurements, as follows

$$c_f^{(i)} = \begin{cases} 1 & (\text{satellite } f \text{ is transmitter of link } i) \& (\text{clock phase jump at satellite } f \text{ occurred during link } i) \\ -1 & (\text{satellite } f \text{ is receiver of link } i) \& (\text{clock phase jump at satellite } f \text{ occurred during link } i) \\ 0 & \text{otherwise} \end{cases} \quad (31)$$

where  $c_f^{(i)}$  is the  $i$ th element of  $\mathbf{c}_f$ . By linearizing the above equation around the ephemeris position  $\bar{\mathbf{X}}$ , we obtain

$$\mathbf{y} = \mathbf{Y} - h(\bar{\mathbf{X}}) \approx \mathbf{H}(\mathbf{X} - \bar{\mathbf{X}}) + \mathbf{c}_f b + \omega = \mathbf{H}\mathbf{x} + \mathbf{c}_f b + \omega \quad (32)$$

where  $\mathbf{y} = \mathbf{Y} - h(\bar{\mathbf{X}})$  and  $\mathbf{x} = \mathbf{X} - \bar{\mathbf{X}}$ , and  $\mathbf{H} \in \mathbb{R}^{m \times 3n}$  is the Jacobian matrix.

For the test, we consider  $n + 1$  hypotheses: The null hypothesis  $\mathcal{H}_0$  where the model errors are absent, and the alternative hypotheses  $\mathcal{H}_1, \dots, \mathcal{H}_n$  which corresponds to the fault satellite being  $f = 1, f = 2, \dots, f = n$ , respectively. The Baarda's  $w$ -test statistic for testing  $\mathcal{H}_0$  against single alternative  $\mathcal{H}_k (k = 1, \dots, n)$  is given as (de Jong & Teunissen, 2014)

$$w_k = \frac{\mathbf{c}_k^\top \Sigma_{yy}^{-1} \mathbf{P}_A^\perp \mathbf{y}}{\sqrt{\mathbf{c}_k^\top \Sigma_{yy}^{-1} \mathbf{P}_A^\perp \mathbf{c}_k}} \quad (33)$$

where the projector  $\mathbf{P}_A^\perp$  is defined as

$$\mathbf{P}_A^\perp = \mathbf{I}_m - \mathbf{H}(\mathbf{H}^\top \Sigma_{yy}^{-1} \mathbf{H})^{-1} \mathbf{H}^\top \Sigma_{yy}^{-1} \quad (34)$$

and

$$c_k^{(i)} = \begin{cases} 1 & \text{satellite } k \text{ is transmitter of link } i \\ -1 & \text{satellite } k \text{ is receiver of link } i \\ 0 & \text{otherwise} \end{cases} \quad (35)$$

Here, we assume that the clock phase jump at satellite  $k$  corrupted all the ISLs that involve satellite  $k$ . The testing procedure is summarized as follows (Imparato et al., 2018).

$$\text{Accept } \mathcal{H}_0 \text{ if } \max_{j \in \{1, \dots, n\}} |w_j| < \sqrt{\chi_\alpha^2(1, 0)} \quad (36)$$

otherwise

$$\text{Accept } \mathcal{H}_k \text{ if } |w_k| = \max_{j \in \{1, \dots, n\}} |w_j| \geq \sqrt{\chi_\alpha^2(1, 0)} \quad (37)$$

The minimum detectable bias for  $\mathcal{H}_k$  is computed as (de Jong & Teunissen, 2014)

$$MDB(k) = \sqrt{\frac{\lambda(\alpha, \gamma, 1)}{\mathbf{c}_k^\top \Sigma_{yy}^{-1} \mathbf{P}_A^\perp \mathbf{c}_k}} \quad (38)$$

Iterating over  $n$  alternate hypotheses using Baarda's  $w$ -test statistic (which is called data snooping) enables the detection of the existence of biases by considering the effect of the biases on the full set of observations. Each test is optimal for any bias magnitude  $b$ , whenever the assumptions of the test are true (Lehmann & Voß-Böhme, 2017). At the same time, it also have several limitations:

1. In  $c_k$ , we assume that the biases are injected into all ISR measurements that contains a satellite with a clock phase jump. However, this assumption is not always true since the clock jumps may have occurred outside the transmission and reception time for some links (the second condition in Equation (31) is not satisfied), based on the satellite link schedule (Iiyama, Vila, & Gao, 2024). This will result in having smaller fault links than the assumed model ( $c_k$ ), and will result in the decreased detection power. If we want to rigorously handle this uncertainty of  $c_k$ , we would need to consider all possible combinations of the links as alternate hypothesis, but this would be computationally intractable.
2. The (approximate) prior information of the satellite positions is needed to compute the Jacobian matrix  $\mathbf{H}$ . For navigation satellite constellations this is not often a problem since at least a coarse ephemeris is available. However, whenever this information is not available, we need to first perform the estimation of the satellite positions from the range measurements. This challenge is especially relevant for LunaNet: its interoperable design will use links to satellites serving other roles (e.g., data relay or scientific missions) that may not broadcast any ephemeris information.

## 4 | PROPOSED CLOCK FAULT DETECTION ALGORITHM USING EUCLIDEAN DISTANCE MATRICES

In this section, we propose a satellite clock fault detection algorithm based on rigid graph theory. The method models the set of inter-satellite range measurements as a weighted graph and analyzes if the set of range measurements is realizable (embeddable) in 3D Euclidean space. Instead of analyzing the realizability of the entire graph, the proposed method analyzes a set of subgraphs to detect faults. The method directly processes the range measurements, and therefore does not require any prior information about the satellite positions or clocks.

The section is structured as follows. First, in section 4.1, we discuss the required topology to detect clock faults based on graph embeddability. In particular, we prove that the graph needs to be vertex redundantly rigid (the minimum graph with such a property in 3D is a fully connected graph of 5 nodes) to detect biases in the range measurements from the graph's embeddability. Next, in section 4.2, we show that the graph's embeddability can be determined by the properties of the geometric centered Euclidean distance matrix (GCEDM), without solving for the position of the nodes. Finally, in section 4.3.2, we propose a fault detection test based on the GCEDM distributions of fully connected subgraphs in the graph.

### 4.1 | Required Graph Topology for Fault Detection

#### 4.1.1 | Definitions

Consider a graph of  $n$  nodes, which corresponds to satellites. Let  $\mathbf{x}_i \in \mathbb{R}^d$ , ( $i \in \{1, \dots, n\}$ ) be the position of the  $i$ th node, and  $\mathbf{X} \in \mathbb{R}^{d \times n}$  be a matrix collecting these points. In this paper, we are interested in the 3D case,  $d = 3$ . In this section and the latter sections, we use the following notation for the range measurements between the two satellites  $i$  and  $j$ , instead of equation (18):

$$r_{ij} = \|\mathbf{x}_i - \mathbf{x}_j\| + f_{ij} + w_{ij} \quad (39)$$

where  $f_{ij} = f_i - f_j$  is the bias of the range measurements added by the clock phase jumps, and  $w_{ij}$  is the measurement noise.

Based on the graph and observed ranges  $r_{ij}$ , we define a weighted graph  $G = \langle V, E, W \rangle$ . A *realization (embedding)* of  $G$  is  $d$ -dimensional Euclidean distance space,  $\mathbb{R}^d$ , is defined as a function  $\Phi$  that maps  $V$  into  $\mathbb{R}^d$ , such that for each edge  $e = (v_i, v_j) \in E$ ,  $W(e) = r_{ij}$  (Jian et al., 2010). A weighted graph  $G = \langle V, E, W \rangle$  is called *d-embeddable* when there is a realization (embedding)  $\Phi : V \rightarrow \mathbb{R}^d$  that maps the edges to points  $(\mathbf{x}_1, \dots, \mathbf{x}_n)$  in  $\mathbb{R}^d$  space.

We define “fault satellite” as a satellite that experiences a clock phase jump, and corrupts at least one range measurement containing itself. A weighted graph is *fault disprovable* if and only if the embeddability of  $G$  implies that it contains no fault satellites, and the non-embeddability of  $G$  implies that it contains at least one fault satellite.

A graph is called *rigid* if it has no continuous deformation other than rotation, translation, and reflection while preserving the relative distance constraints between the vertices (Laman, 1970). Otherwise, it is called a *flexible* graph. A graph is called *k-vertex redundantly rigid* if it remains rigid after removing any  $(k - 1)$  vertices.

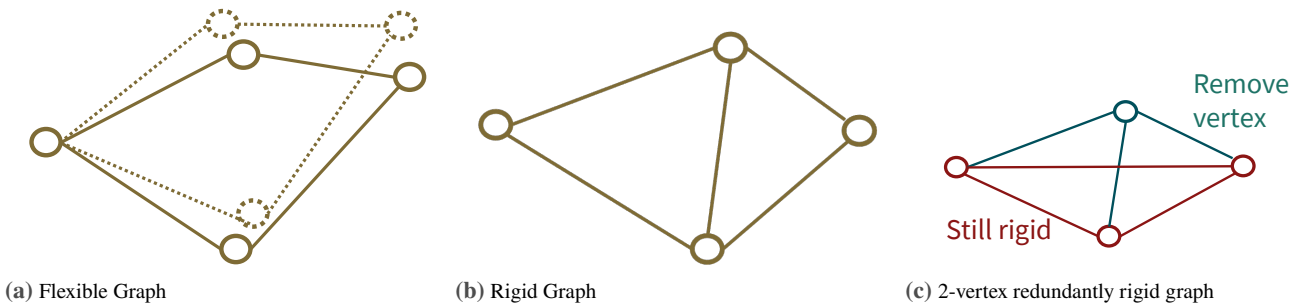


Figure 3 Flexible, Rigid, and 2-vertex redundantly rigid graphs in  $\mathbb{R}^2$

#### 4.1.2 | Embeddability of Graphs with Fault Satellites

In this section, we prove the sufficient condition for the graph to be fault disprovable in  $\mathbb{R}^d$ . For the proofs of this subsection only, we ignore the noise added to the measurements.

**Proposition 4.1.** *Suppose there is at most  $k - 1$  fault satellite on a graph  $G = \langle V, E, W \rangle$  that is  $k$ -vertex ( $k \geq 2$ ) redundantly rigid in  $\mathbb{R}^d$ . If  $G$  is  $d$ -embeddable, then  $G$  contains no fault vertex (satellite) with probability 1.*

*Proof.* See Appendix B. □

**Proposition 4.2.** *Given a weighted graph  $G$ , if  $G$  is  $k$ -vertex redundantly rigid ( $k \geq 2$ ), then  $G$  is fault disprovable at probability 1, if there are at most  $k - 1$  fault satellites.*

*Proof.* For an arbitrary graph  $G$ , if  $G$  is not embeddable, then  $G$  contains at least one fault satellite. Therefore, with Proposition 4.1, if  $G$  is  $k$ -vertex redundantly rigid ( $k \geq 2$ ), then  $G$  is fault disprovable at probability 1, if there are at most  $k - 1$  fault satellites. □

## 4.2 | Properties of the Euclidean Distance Matrix

In the previous section, we proved that by using vertex redundantly rigid graphs, we can detect faults by analyzing their embeddability. Analyzing the embeddability of an arbitrary graph is known to be NP-hard (Hendrickson, 1992), but if the graph is fully connected, we can evaluate it by analyzing the ranks of the GCEDM. Note that fully connected graphs of more than 5 nodes are 2-vertex redundantly rigid in  $\mathbb{R}^3$ .

In this section, we introduce and prove several properties of the EDM and GCEDM constructed from the observed ranges between the satellites. We show how we can use the singular values of the GCEDM to evaluate if a (fully-connected) (sub)graph is embeddable in  $\mathbb{R}^3$ .

#### 4.2.1 | Geometric Centered Euclidean Distance Matrix

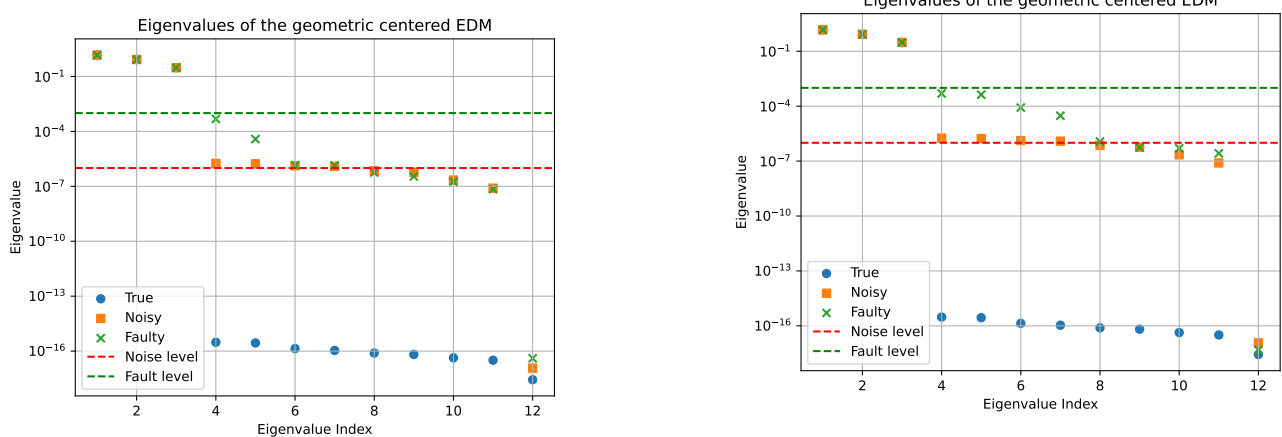
Using the set of observed ranges  $r_{ij}$ , we construct an EDM, where its elements are equivalent to the square of the observed ranges ( $r_{ij}^2$ ).

Let  $\mathbf{D}^{n,d,m} \in \mathbb{R}^{n \times n}$  be an EDM without measurement noise ( $w_{ij} = 0$ ) and  $m$  nodes out of  $n$  nodes being fault. For example, a noiseless EDM with 6 satellites (in 3D space) with 2 fault satellites is denoted as  $\mathbf{D}^{6,3,2}$ . Similarly, we define  $\tilde{\mathbf{D}}^{n,d,m} \in \mathbb{R}^{n \times n}$  as EDM with measurement noise and  $m$  nodes out of  $n$  nodes having a fault. A GCEDM  $\mathbf{G}^{n,d,m}$  (or  $\tilde{\mathbf{G}}^{n,d,m}$  for noisy EDM  $\tilde{\mathbf{D}}^{n,d,m}$ ) is constructed from the EDM from the following operation

$$\mathbf{G}^{n,d,m} = -\frac{1}{2} \mathbf{J}^n \mathbf{D}^{n,d,m} \mathbf{J}^n \quad (40)$$

where  $\mathbf{J}^n$  is the geometric centering matrix as follows.

$$\mathbf{J}^n = \mathbf{I}^n - \frac{1}{n} \mathbf{1} \mathbf{1}^\top \quad (41)$$



(a) Singular values of the geometric centered EDM with one fault satellite. The fourth and fifth singular values increase compared to the non-fault case when the fault magnitude is sufficiently larger than the noise magnitude.

(b) Singular values of the geometric centered EDM with two fault satellites. The fourth, fifth, sixth, and seventh singular values increase compared to the non-fault case when the fault magnitude is sufficiently larger than the noise magnitude.

**Figure 4** The log plot of the singular values of an example geometric centered EDM for  $n = 12, d = 3$ . The singular values are ordered in the descending order of its magnitude. The blue circles show the singular values when there is no fault or noise ( $\mathbf{G}^{12,3,0}$ ), the orange squares show the singular values when there is noise (of scale  $\sigma_w = 10^{-6}$ ) added to the range measurements ( $\tilde{\mathbf{G}}^{12,3,0}$ ), and the green crosses show the singular values when both noise and fault (of scale  $\bar{b} = 10^{-3}$ ) is added ( $\tilde{\mathbf{G}}^{12,3,2}$ ). The 12 points are identical for all cases, which are sampled randomly inside a unit cube. When noise is present, the singular values increase except for the last singular value, which is close to zero (theoretically zero). When  $m$  faults with magnitudes that are larger than the noise magnitude are added, the singular values up to the  $d + 2m$  index increase compared to the non-fault case.

where  $\mathbf{1} \in \mathbb{R}^n$  is the ones vector. When no fault or noise is present ( $m = 0$ ), the  $\mathbf{G}^{n,d,0}$  will be positive semi-definite, and its rank will satisfy  $\text{rank}(\mathbf{G}^{n,d,0}) = \text{rank}(\mathbf{X}^\top \mathbf{X}) \leq d$  (Dokmanić et al., 2015).

#### 4.2.2 | Rank of the Euclidean Distance Matrices with Fault Satellites

Knowles and Gao (2023) observed that there are more than three nonzero singular values when the GCEDM is constructed from an EDM with fault satellites. An example is provided in Figure 4. However, mathematical proofs were not provided in their paper. In this section, we provide and prove several properties of the EDM and GCEDM that are corrupted with faults and measurement noises.

**Proposition 4.3.** *The rank of the EDM  $\mathbf{D}^{n,d,m}$  satisfies*

$$\text{rank}(\mathbf{D}^{n,d,m}) \leq \min(d + 2 + 2m, n) \quad (42)$$

*Proof.* See Appendix C. □

**Proposition 4.4.** *The rank of the GCEDM  $\mathbf{G}^{n,d,m} = -\frac{1}{2}\mathbf{J}^n \mathbf{D}^{n,d,m} \mathbf{J}^n$  satisfies*

$$\text{rank}(\mathbf{G}^{n,d,m}) \leq \min(d + 2m, n - 1) \quad (43)$$

*Proof.* See Appendix D. □

**Corollary 4.4.1.** *The GCEDM  $\tilde{\mathbf{G}}^{n,d,m} = -\frac{1}{2}\mathbf{J}_n \tilde{\mathbf{D}}^{n,d,m} \mathbf{J}_n$  constructed from an EDM with the edges corrupted by Gaussian noise almost surely has rank*

$$\text{rank}(\tilde{\mathbf{G}}^{n,d,m}) = n - 1 \quad (44)$$

*Proof.* See Appendix E. □

#### 4.2.3 | Distribution of the 4th Singular Value of the Geometric Centered EDM

The propositions proved in the previous sections indicate that we can detect fault satellites by observing the increase in the 4th singular value (since the dimension is 3) of the GCEDMs constructed from the ISR measurements. We use the following test statistic  $\gamma_{\text{test}}$  to monitor if a fault satellite exists in a given subgraph.

$$\gamma_{\text{test}} = \lambda_4^2 \quad (45)$$

where  $\lambda_i$  is the  $i$ th singular value of the geometric centered EDM. If the ISR measurements are completely noiseless, we can detect if a fault satellite exists within the graph by checking if  $\gamma_{\text{test}}$  of the GCEDMs is not 0, since GCEDMs have rank 3 when no fault exists. However, when the ISR measurements are noisy, the 4th singular value increase regardless of faults, as shown in Figure 4 and Corollary 4.4.1. Therefore, to detect faults under the presence of noises, we need to set a threshold based on the singular value distributions of the noisy (but non-fault) GCEDMs to separate the fault from the noise.

For  $n = 5$ , we are able to compute the distribution of the test statistic analytically. The distribution of the test statistic  $\gamma_{\text{test}}/s$  follows a centralized chi-squared distribution with degree of freedom 1, as follows:

$$\frac{\gamma_{\text{test}}}{s} \sim \chi^2(1, 0) \quad \text{for } n = 5 \quad (46)$$

where the scale  $s$  is given by the following equation:

$$s = 2 \sum_{i=1}^5 \sum_{j=1}^5 \left( \sigma_m \tilde{\mathbf{D}}_{ij} \right)^2 \cdot \|\hat{\mathbf{U}}_{i,:}\|^2 \cdot \|\hat{\mathbf{V}}_{j,:}\|^2 \quad \hat{\mathbf{U}}_{i,:}, \hat{\mathbf{V}}_{j,:} : i\text{th and } j\text{th row of } \hat{\mathbf{U}}, \hat{\mathbf{V}} \in \mathbb{R}^{5 \times 2} \quad (47)$$

$$\hat{\mathbf{U}} = \mathbf{J}_5 \tilde{\mathbf{U}}_{:,4:5} \in \mathbb{R}^{5 \times 2} \quad \tilde{\mathbf{U}}_{:,4:5} : 4\text{th and } 5\text{th column of } \tilde{\mathbf{U}} \in \mathbb{R}^{5 \times 5} \quad (48)$$

$$\hat{\mathbf{V}} = \mathbf{J}_5 \tilde{\mathbf{V}}_{:,4:5} \in \mathbb{R}^{5 \times 2} \quad \tilde{\mathbf{V}}_{:,4:5} : 4\text{th and } 5\text{th column of } \tilde{\mathbf{V}} \in \mathbb{R}^{5 \times 5} \quad (49)$$

$$\tilde{\mathbf{U}} \tilde{\Sigma} \tilde{\mathbf{V}}^\top = \text{SVD}(\tilde{\mathbf{G}}) \quad \text{SVD : Singular Value Decomposition, } \gamma_{\text{test}} = \tilde{\Sigma}_{4,4}^2 = (\lambda_4)^2 \quad (50)$$

Above,  $\tilde{\mathbf{G}}, \tilde{\mathbf{D}} \in \mathbb{R}^{5 \times 5}$  are the (noisy) GCEDM and the distance matrix constructed from the measured ranges, respectively. The derivation is given in Appendix F. The scale of the distribution is proportional to the noise magnitude  $\sigma_m^2$  (Figure 5). Equation (47) can be modified to compute the scale when the variance of noise is different for each measurement, by replacing  $\sigma_m$  with  $(\sigma_m)_{ij}$  (the noise for each range measurement).

When there is a clock jump at satellite  $s_f$ , the distribution of the test statistic  $(\gamma_{\text{test}})_{s_f}$  follows a non-central chi-squared distribution with 1 degree of freedom, with its scale  $s$  given by the same equation as above, and non-centrality parameter  $\lambda_{s_f}$ :

$$\frac{(\gamma_{\text{test}})_{s_f}}{s} \sim \chi^2(1, \lambda_{s_f}) \quad \text{for } n = 5 \quad (51)$$

where the non-centrality parameter  $\lambda_{s_f}$  is given by the following equation:

$$\lambda_{s_f} = \frac{1}{s} \|\hat{\mathbf{U}}^\top (\mathbf{F} \circ \mathbf{D}) \hat{\mathbf{V}}\|_F^2 \quad (52)$$

$$\mathbf{F} = \begin{cases} f_{ij} & i = s_f \text{ or } j = s_f \\ 0 & \text{otherwise} \end{cases} \quad (53)$$

Therefore, when all biases added by faults have the same magnitude, the non-centrality parameter  $\lambda$  is proportional to the square of the fault magnitude as shown in Figure 6 and Figure 7. The derivation is given in Appendix G.

Using equations (46) and (51), we can compute the minimum detectable bias for satellite  $i$  as follows:

$$MDB(i) = \sqrt{\lambda_i \cdot s}, \quad P[\chi^2(1, \lambda_i) \leq \chi_\alpha^2(1, 0)] = 1 - \gamma \quad (54)$$

where  $\alpha$  is the false alarm rate,  $\gamma$  is the detection power,  $s$  is the scale, provided in (47), and  $\lambda_i$  is the non-centrality parameter for satellite  $i$  fault case, provide in equation (52).

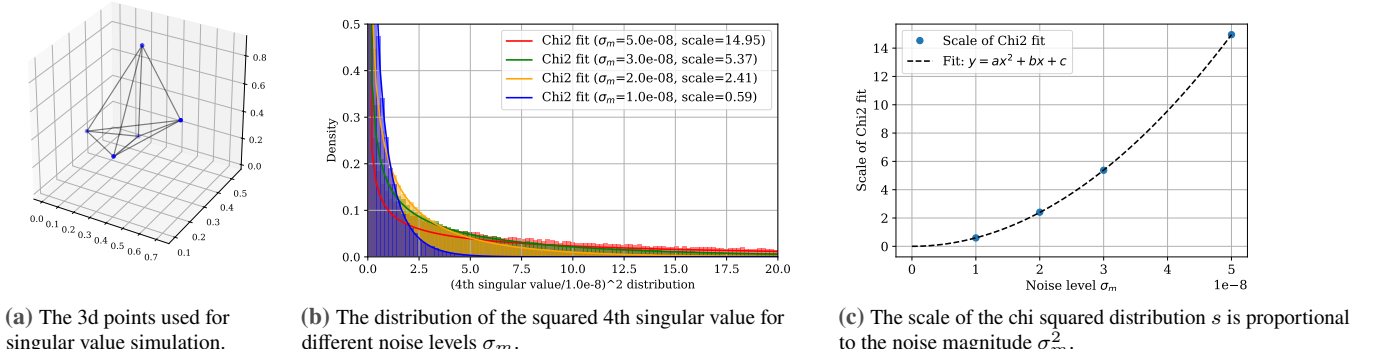


**Figure 5** The distribution of the test statistic  $\gamma_{\text{test}}$  and its scale  $s$  for different noise levels  $\sigma_m$ . The distribution of the test statistic  $\gamma_{\text{test}}$  follows a chi-squared distribution with 1 degree of freedom. The scale  $s$  is proportional to the noise magnitude  $\sigma_m^2$ .

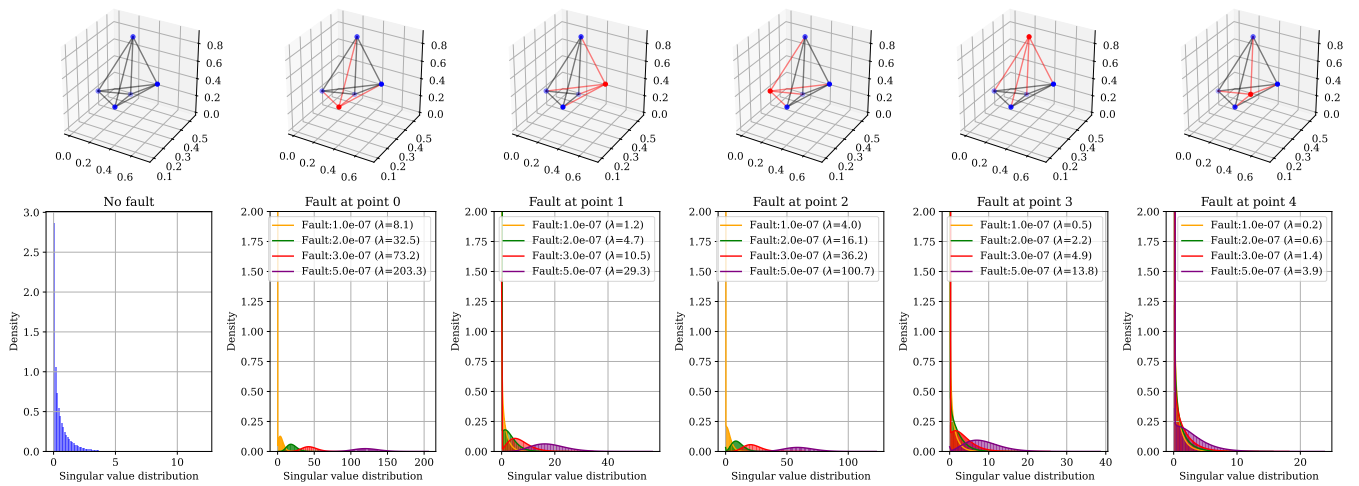


**Figure 6** The distribution of the test statistic  $\gamma_{\text{test}}$  for different fault magnitudes and fault satellites. The top row shows the points in 3d space, where the red points and edges indicate the fault satellite and its connected edges, respectively. The distribution of the test statistic  $\gamma_{\text{test}}$  follows a non-central chi-squared distribution with 1 degree of freedom. The non-centrality parameter  $\lambda$  becomes larger as the fault magnitude increases.

## 4.3 | Fault Detection Algorithm Using Euclidean Distance Matrix

### 4.3.1 | Clique Listing

In order to construct an EDM and GCEDM, we need a set of range measurements between all pairs of  $n$  satellites. However, due to the occultation by the planetary body and attitude constraints, the satellites in the constellation are not fully connected with ISRs in most cases. Therefore, the first step of the fault detection algorithm is to find a set of  $k$ -clique subgraphs, which are fully connected subgraphs of  $k$  satellites. For the graph to be 2-vertex redundantly rigid, and to use the derived distribution (46), we are interested in cliques with  $k = 5$ . An example of 5-cliques subgraphs is shown in Figure 8.

Various exact algorithms to find all  $k$ -cliques have been proposed (Li et al., 2020). In this paper, we used the Chiba-Nishizeki Algorithm (Albo) due to its simplicity of implementation (Chiba & Nishizeki, 1985). For each node  $v$ , Arbo expands the list of  $k$ -cliques by recursively creating a subgraph induced by  $v$ 's neighbors. The readers are referred to (Li et al., 2020) for the pseudocode and summary of the  $k$ -clique listing algorithm. Note that the clique finding algorithm does not have to be executed online. Since the availability of the ISRs can be predicted beforehand when scheduling the ISLs using a coarse predicted orbit, we can estimate the topology of the ISLs for future time epochs. We can compute the list of  $k$ -cliques of the predicted topologies for

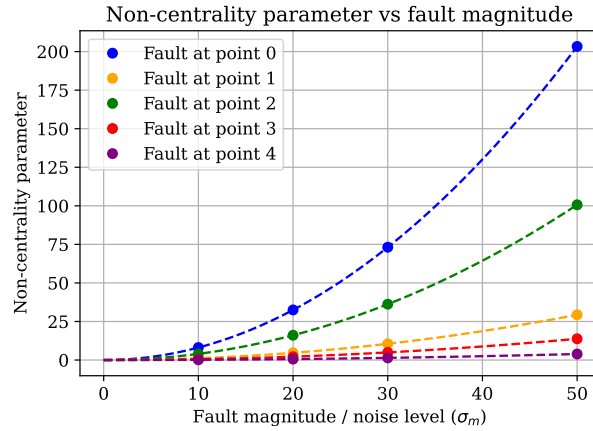
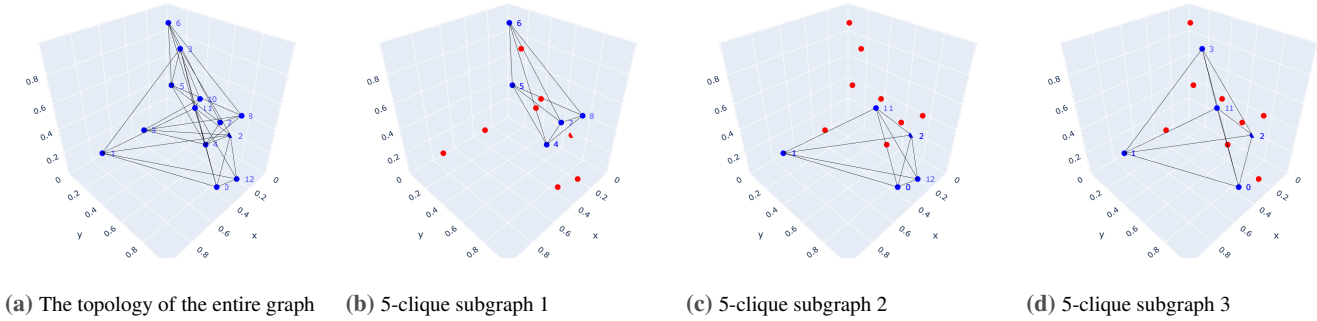


Figure 7 The non-centrality parameter  $\lambda$  of the distribution of the test statistic is proportional to the square of the fault magnitude  $\bar{b}^2$ .

future time epochs (e.g., one orbit), and uplink them to satellites intermittently. If some of these links were actually not available in orbit for some reason, we can remove the  $k$ -cliques that contain the missing links from the list.



(a) The topology of the entire graph (b) 5-clique subgraph 1 (c) 5-clique subgraph 2 (d) 5-clique subgraph 3

Figure 8 Listing 5-cliques within the graph of 13 nodes that are not fully connected.

### 4.3.2 | Online Fault Detection

We define the “fault satellite” as the satellite that has a clock jump, and the “fault-free satellite” as the satellite that does not have a clock jump. We design a test where we consider the following hypotheses:

$$\begin{aligned} H_0 &: \text{All satellites are fault-free (null hypothesis)} \\ H_i &: \text{The satellite } i \text{ is a fault satellite} \end{aligned} \quad (55)$$

Let  $\mathcal{L}_t^G$  be the list of all 5-cliques of the satellite network as a graph at time step  $t$ , and  $N_s$  the total number of satellites. We propose an online fault detection algorithm, which uses  $\mathcal{L}_t^G$ . The procedure of the detection algorithm is as follows.

#### Algorithm:

1. First, we compute the scaled test statistic  $\gamma_{test,G'} = \lambda_4^2/s$  for each 5-clique subgraph  $G'$  in  $\mathcal{L}_t^G$ , using Eq.(47).
2. For each satellite  $i$  in the graph, repeat the following steps (a) to (c):
  - (a) Compute the sum of all the scaled test statistics for subgraphs that do not include satellite  $i$ .

$$\gamma_{test}^i = \sum_{G' \in \mathcal{L}_t^G, i \notin G'} \gamma_{test,G'}. \quad (56)$$

(b) Compute the threshold  $\bar{\gamma}_{\text{test}}^i$  for the sum of the scaled test statistics  $\gamma_{\text{test}}^i$  for a given false alarm rate  $\alpha$  and (user-defined) threshold margin  $\eta_\alpha$ .

$$\bar{\gamma}_{\text{test}}^i = \eta_\alpha \cdot \chi_\alpha^2(N_{G,i}, 0) \quad (57)$$

where  $N_{G,i}$  is the number of subgraphs that do not include satellite  $i$ ,  $\eta_\alpha$  is the threshold margin, and  $\chi_\alpha^2(N_{G,i}, 0)$  is the  $\alpha$ -quantile of the central chi-squared distribution with  $N_{G,i}$  degrees of freedom.

(c) Normalize the test statistic by dividing it by the threshold  $\bar{\gamma}_{\text{test}}^i$ .

$$\gamma_{\text{test}}^i = \frac{\gamma_{\text{test}}^i}{\bar{\gamma}_{\text{test}}^i}. \quad (58)$$

3. If for all satellite  $i$  we have  $\gamma_{\text{test}}^i < 1$ , we accept the null hypothesis, and otherwise we reject the null hypothesis. We identify the fault satellite  $s_f$  as the one with the smallest  $\gamma_{\text{test}}^i$ .

$$s_f = \operatorname{argmin}_i \gamma_{\text{test}}^i \quad (59)$$

The proposed fault detection algorithm has two hyperparameters that affect its performance.

False Alarm Rate  $\alpha$ : This is the probability of a false alarm, which is the probability of detecting a satellite as faulty when it is actually fault-free.

Threshold Margin  $\eta_\alpha$ : This inflates the threshold  $\bar{\gamma}_{\text{test}}$  to  $\eta_\alpha \cdot \bar{\gamma}_{\text{test}}$ , to account for the increase in the variance of the sum of the test statistics, due to the correlation between the test statistics of the subgraphs.

We need to set the threshold margin  $\eta_\alpha$  to a value larger than 1, to account for the increase in the variance of the distribution of  $\gamma_{\text{test}}^i$ . Due to the correlation between the test statistics of the subgraphs. The correlation between the test statistics of the subgraphs is caused by the fact that the same set of range measurements is used to compute the test statistics between different subgraphs. We compute the test statistics for subgraphs that do not contain satellite  $i$ , instead of subgraphs that contain  $i$ , to avoid having strong correlations between the test statistics of the subgraphs, which would require a larger threshold margin  $\eta_\alpha$ .

Note that the above test only considers a maximum of one fault satellite. One possible extension to the test to consider multiple fault satellites is to run the algorithm iteratively, removing the detected fault satellite from the graph after each iteration until no fault is detected (**knowles2024greedy**). Alternatively, we can consider  $N_s C_{N_f}$  combinations of fault satellites, where  $N_f$  is the number of fault satellites, and compute the test for each combination. The detection performance in the case of multiple faults will be performed in future work.

## 5 | SATELLITE FAULT DETECTION SIMULATION

### 5.1 | Simulation Configuration

#### 5.1.1 | Orbits and Links

To validate the proposed fault detection algorithm, we consider the following two constellations.

1. GPS constellation of 31 satellites: The satellite orbits are initialized using the Two-Line Element (TLE) data from 2025/4/3 from the Celestrak website (**celestak'gp'data'formats'2025**). The 3-dimensional plots of the constellation and the available ISLs at  $t = 0$  are shown in Figure 10(a).
2. A notational lunar constellation of 17 satellites: We considered a hybrid constellation, where 9 satellites form a 9/3/1 Walker-Delta constellation and 8 satellites are deployed in elliptical lunar frozen orbits (ELFO). The constellation is based on the design proposed by **kang2025design<empty citation>**, which provides a good coverage of the lunar south pole, while maintaining a good global coverage. The orbital elements of the constellation are shown in Table 1, and the 3-dimensional plots of the constellation and the available ISLs at  $t = 0$  are shown in Figure 11(a).

For both constellations, the orbits are propagated in the two-body propagator without considering perturbations. The availability of the links is calculated assuming that the links are available when it is not occulted by the central body, and the angle between the line of sight and the satellite-body center vector is less than  $\phi_{\max}$ , as illustrated in Figure 9. The cutoff angle  $\phi_{\max}$  is set to 60 degrees for the Earth case (Zhang et al., 2024) and 80 degrees for the Moon case. To compute body occultation, we set an additional mask of 1000 km for the Earth case, and 100 km for the Moon case to avoid the link being corrupted by ionospheric

delays or terrain blockage. We assume that we can obtain the range measurements from all available links at each time step. The scheduling of the links will be investigated in future work.

The number of 5 cliques in the constellation with the number of subgraphs containing PRN 1, 10, and 15 is shown in Figure 10(b) and Figure 11(b) for the Earth and Moon cases, respectively. For the lunar constellation, the ELFO satellites have time windows where they have no self-contained subgraphs, where the faults at the satellite cannot be detected using the EDM method.

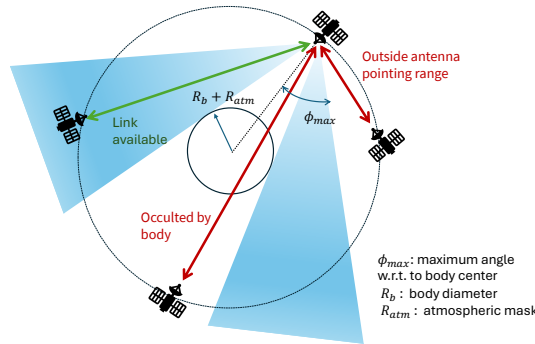
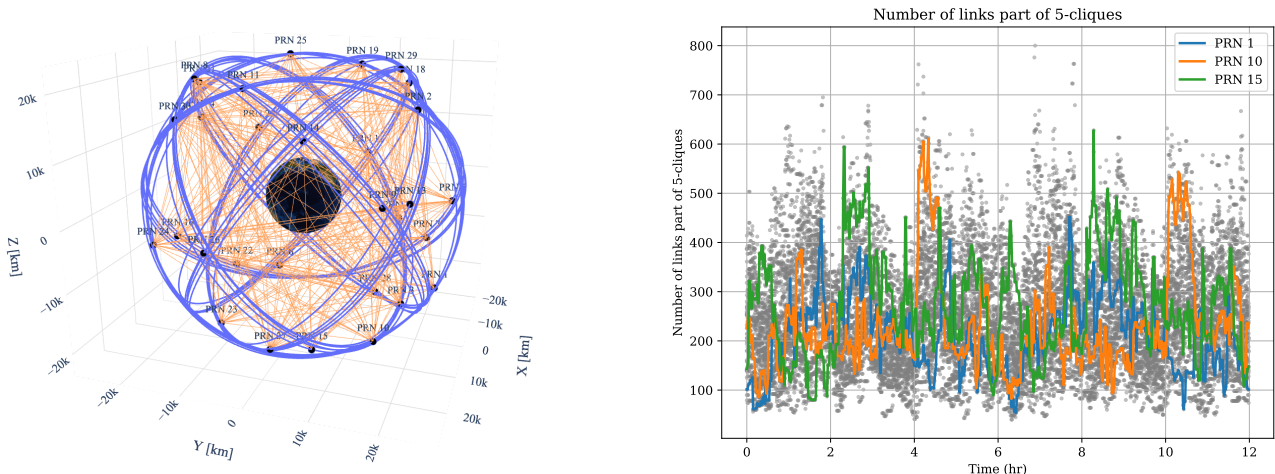


**Figure 9** The visibility of the link between two satellites is calculated assuming that the link is visible when it is not occulted by the central body (including the atmospheric mask), and the angle between the line of sight and the satellite-body center vector is less than  $\phi_{max}$ .



**(a)** Orbital planes with satellite position (black points) and links (orange line) at the initial time epoch. The constellation consists of 31 satellites, 9 of which are in the Walker constellation with 3 planes (shown in blue), and 8 satellites are in the 2 ELFO planes (shown in red).

**(b)** The scatter plot of the number of 5-cliques for each satellite in the constellation over full orbit. The number of 5-cliques that contain PRN 1, 10, and 15 are shown in blue, orange, and green, respectively. Each satellite has more than 30 self-containing subgraphs throughout the orbit.

**Figure 10** A GPS constellation around Earth with 31 satellites. The orbit is initialized using the TLE data from CelesTrak.

### 5.1.2 | Parameters

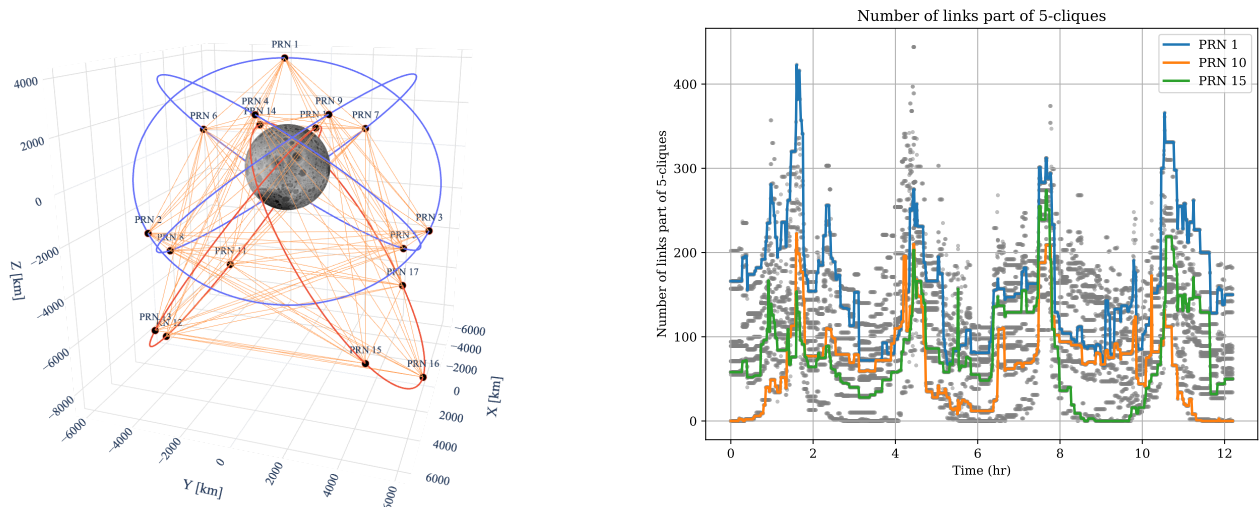
We tested combinations of different detection and simulation parameters:

- Test methods: ‘Sum of residuals’, ‘Data snooping’, and ‘EDM’
- Fault magnitudes:  $\bar{b} = 1, 2, 5, 10, 20$  m

**Table 1**

Orbital elements of the Waker/ELFO hybrid lunar constellation (Case 2)

Plane	PRN	Semi-Major Axis	Eccentricity	Inclination	RAAN	Argument of Periapsis	Mean Anomaly
		$a$ [km]	$e$ []	$i$ [deg]	$\Omega$ [deg]	$\omega$ [deg]	$M$ [deg]
1	1 - 3	6215.0	0.0	39.2	110	90	[0, 120, 240]
2	4 - 6	6215.0	0.0	39.2	230	90	[40, 160, 280]
3	7 - 9	6215.0	0.0	39.2	350	90	[80, 200, 320]
4	10 - 13	6215.0	0.7	55.0	0	90	[0, 90, 180, 270]
5	14 - 17	6215.0	0.7	55.0	180	90	[0, 90, 180, 270]



(a) Orbital planes with satellite position (black points) and links (orange line) at the initial time epoch. The constellation consists of 17 satellites, 9 of which are in the Walker constellation with 3 planes (shown in blue), and 8 satellites are in the 2 ELFO planes (shown in red).

(b) The scatter plot of the number of self-containing 5-cliques for each satellite in the constellation over full orbit. The number of 5-cliques that contain PRN 1, 5, and 15 are shown in blue, orange, and green, respectively. The satellites in ELFO (PRN 10 - 17) experience a time window near the periapsis where they have zero 5-cliques, where faults on that satellite cannot be detected.

**Figure 11** A hybrid lunar constellation around the Moon with 17 satellites

- Ratio of fault links (the probability that the link connected to a fault satellite is biased):  $r_f = 0.2, 1.0$
- Number of fault satellites:  $N_f = 0, 1$ .
- False alarm rates for the fault detection algorithms:  $\alpha = 0.001, 0.01, 0.05$

For each of these cases, we run 5000 Monte-Carlo analyses with randomly sampled initial times (within one orbital period) and a set of fault satellites. For all cases, we set the standard deviation of the two-way noise measurement error to  $\sigma_m = 0.5$  m, based on the results of the Beidou constellation (Zhang et al., 2024), and used  $\eta_\alpha = 1.5$  for the threshold margin.

### 5.1.3 | Evaluation Metrics

We compute the following metrics to evaluate the performance of the fault detection algorithm

$$\text{True Positive Rate or Recall (TPR)} = \frac{TP}{TP + FN} \quad (60)$$

$$\text{False Positive Rate (FPR)} = \frac{FP}{FP + TN} \quad (61)$$

$$P_4 \text{ metric (} P_4 \text{)} = \frac{4 \cdot TP \cdot TN}{4 \cdot TP \cdot TN + (TP + TN) \cdot (FP + FN)} \quad (62)$$

where  $TP, FN, FP, TN$  is the total number of true positives (fault satellite classified as fault), false negatives (fault satellite classified as non-fault), false positives (non-fault satellite classified as fault), and true negatives (non-fault satellite classified as non-fault). A higher TPR is desired not to miss fault satellites, and a lower TPR is desired to prevent false alarms, detecting normal satellites as a fault.  $P_4$  value is the harmonic mean of four key conditional probabilities (precision, recall, specificity, and negative predictive value), where  $P_4 = 1$  requires all of these values to be 1 (Sitarz, 2023).  $P_4$  value could be used as a metric to evaluate the “balance” between these metrics.

## 5.2 | Fault Detection Results

### 5.2.1 | Case 1: GPS Constellation

The fault detection results for the GPS constellation with different combinations of parameters are shown in Figure 12. When there are no fault satellites, FPRs of all methods are lower than the user-defined threshold  $\alpha = 0.001, 0.01, 0.05$ . The sum of residuals method and the EDM method show the lowest FPR, due to their conservative threshold setting (assuming maximum correlation between the residuals for the sum of residuals method, and inflating the threshold for the EDM method).

The TPR and FPR of the sum of residuals method improve as the ephemeris accuracy improves, as shown in Figure 12(b) - 12(d). When the ephemeris accuracy is high ( $\sigma_m = 1$  m), the algorithm achieves nearly perfect fault detection when the fault magnitude is larger than 5 m, while with lower accuracy ( $\sigma_m = 3$  m), it will require a larger fault magnitude (10 m) to achieve the same TPR.

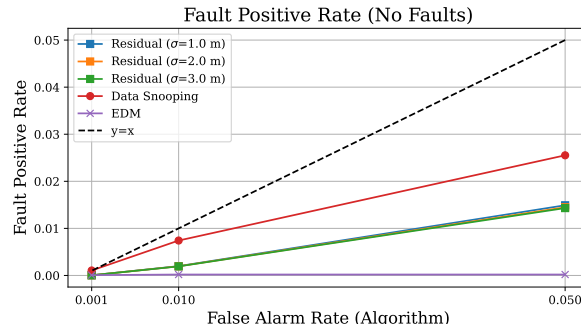
When the fault ratio is 1 (all ISRs containing fault satellites are corrupted), the data snooping method performs the best among the three methods, due to its optimality of the test. The EDM method also showed TPR over 0.7 for a fault magnitude of 2 m, marking a better P4 score than the sum of residuals method.

However, when the fault ratio is 0.2 (a smaller number of links are biased by the clock jump, such as due to link scheduling), the data snooping method showed worse TPR than the EDM method and the sum of residuals method with  $\sigma_m = 1$  m, since the data snooping test assumes all fault-satellite containing ISRs are biased. The data snooping method also showed worse FPR as the fault magnitude increases. For a fault ratio of 0.2, the EDM method showed the highest P4 score at fault magnitudes  $\leq 10$  m, while the sum of residuals method showed the highest P4 score at fault magnitudes  $\geq 10$  m.

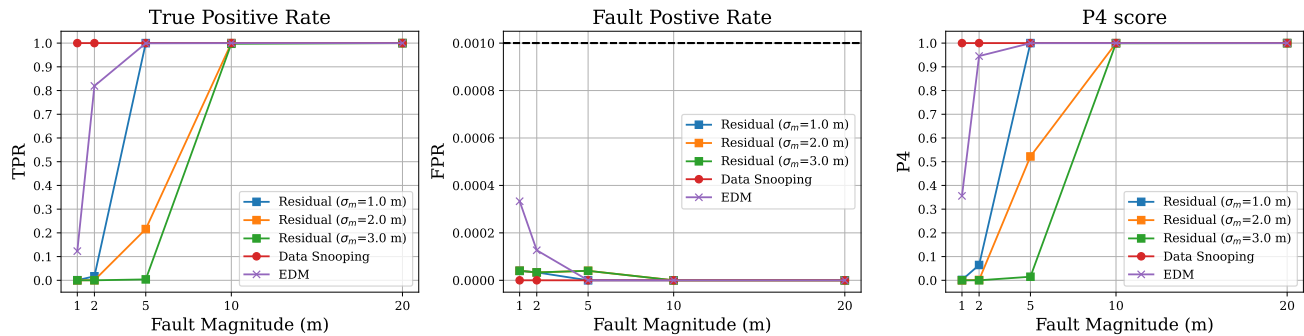
### 5.2.2 | Case 2: Lunar Constellation

The metrics for the lunar cases are shown in Figure 13. Similar to the Earth GPS case, when there is no fault, the FPR of all methods are lower than the user-defined threshold  $\alpha = 0.001, 0.01, 0.05$ , and the TPR and FPR of the sum of residuals method improve as the ephemeris accuracy improves and the fault magnitude increases.

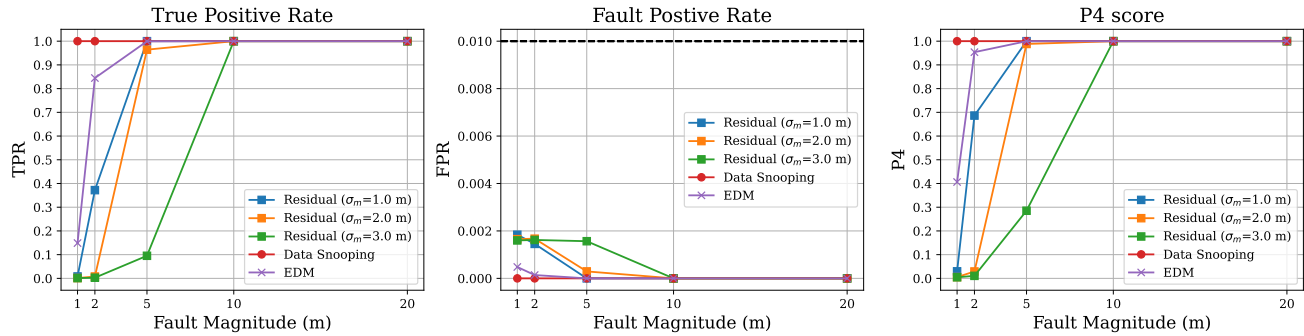
When the fault ratio is 1, the TPR of the EDM and the data snooping methods caps around 0.91, due to the small number of available links near the perilune for the ELFO satellites, making the test statistic less sensitive to the bias. When the fault magnitudes are larger ( $\geq 10$  m), the sum of residuals method shows larger TPR and lower FPR than the other two methods, since the method directly compares the observed range to the expected range, and thus the performance does not depend on the overall geometry of the links (i.e., or the observability of the bias in the system). When the fault ratio is 0.2 (a smaller number of links are biased by the clock jump), the EDM method shows the highest P4 score at fault magnitudes  $\leq 10$  m, while the sum of residuals method shows the highest P4 score at fault magnitudes  $\geq 20$  m. Overall, the EDM method shows the most balanced performance (P4 score) over different fault magnitudes and fault ratios for the lunar case.



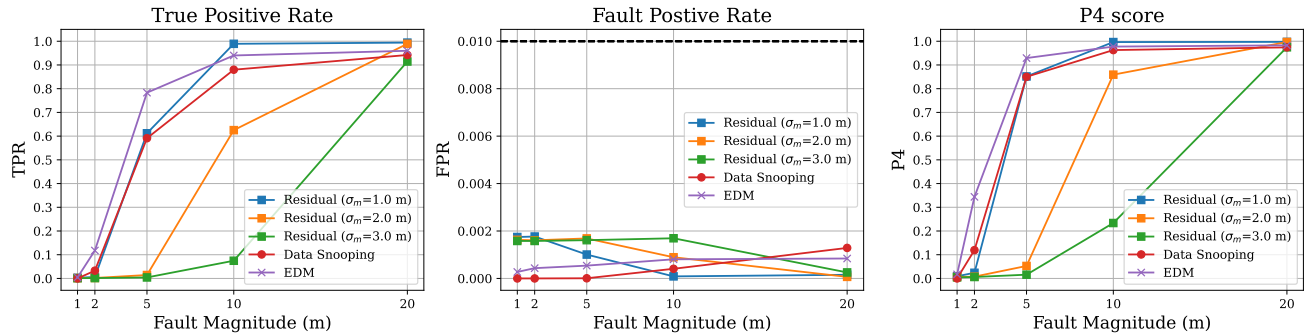
(a) The results for the Earth case with no faults.



(b) The results for the Earth case with 1 fault satellite, a false alarm rate of 0.001, and a fault ratio of 1.



(c) The results for the Earth case with 1 fault satellite, a false alarm rate of 0.01, and a fault ratio of 1.



(d) The results for the Earth case with 1 fault satellite, a false alarm rate of 0.01, and a fault ratio of 0.2.

**Figure 12** The fault detection results for the Earth case with 0 or 1 fault satellite. When there is no fault, the FPR for all methods went below the user-defined threshold  $\alpha = 0.001, 0.01, 0.05$ . The TPR and FPR of the sum of residuals method improve as the ephemeris accuracy improves and the fault magnitude increases. When the fault ratio equals 1, the data snooping has better TPR and FPR at lower fault magnitudes due to the optimality of the test. However, when the fault ratio is 0.2 (a smaller number of links are biased by the clock jump), the TPR of the data snooping method becomes worse than the other methods, since the test assumes all fault-satellite containing ISRs are biased.

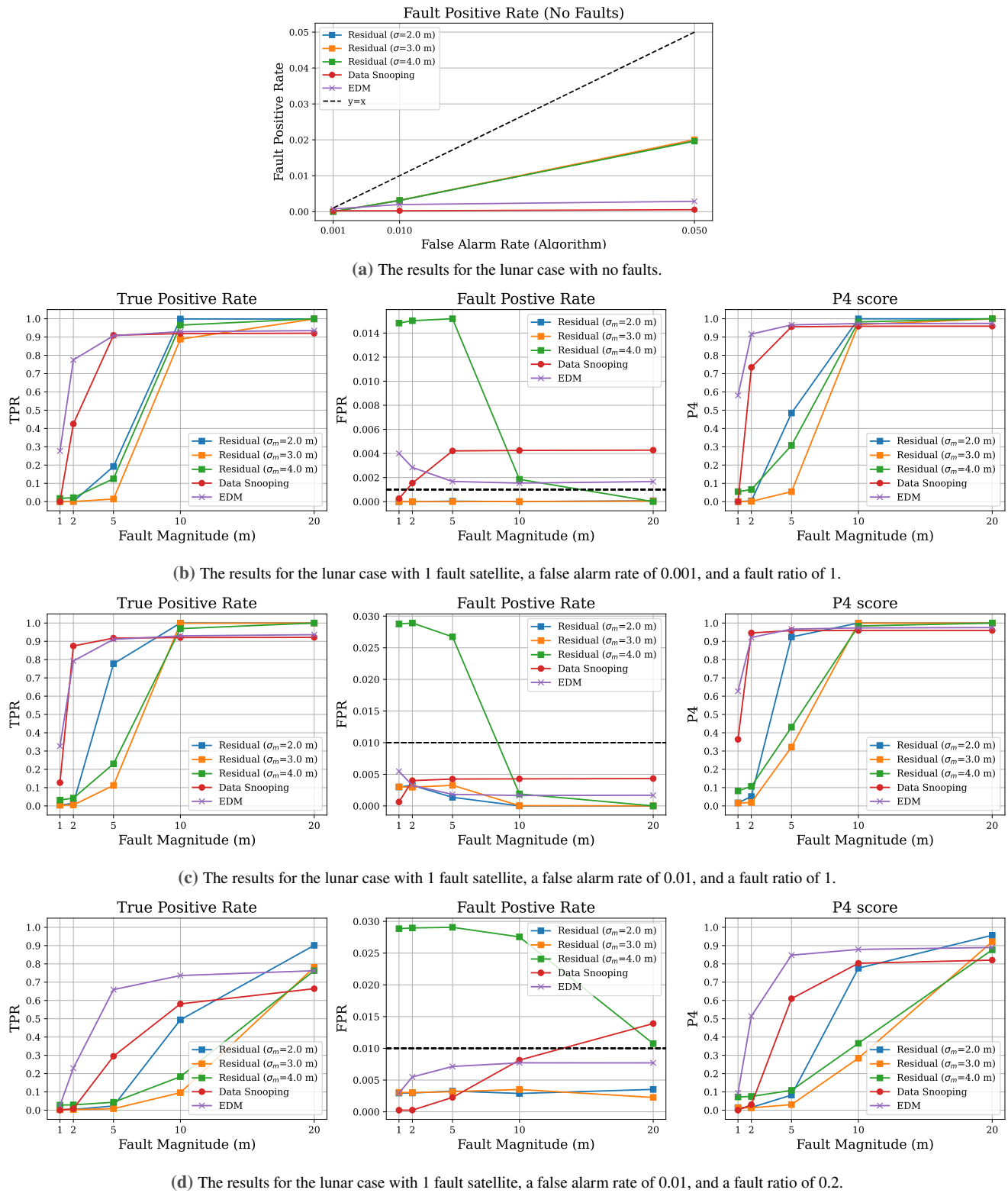


**Figure 13** The fault detection results for the lunar case with 0 or 1 fault satellite. When there is no fault, the FPR of all methods went below the user-defined threshold  $\alpha = 0.001, 0.01, 0.05$ . The TPR of the EDM and the data snooping methods caps around 0.91, due to the small number of available links near the perilune for the ELFO satellites making the test statistic less sensitive to the bias (the bias becoming less observable in the linear system). When the fault ratio is 0.2 (a smaller number of links are biased by the clock jump), the EDM method shows the highest P4 score at fault magnitudes  $\leq 10$ m, while the sum of residuals method shows the highest P4 score at fault magnitudes  $\geq 20$ m.

## 6 | CONCLUSION

In this paper, we proposed a new clock phase jump detection algorithm for satellite constellations using ISR measurements. The method can operate autonomously within the constellation. In addition, since the fault detection directly processes the measurement ISR measurements, it does not require prior knowledge of the satellite positions or clock biases, offering a flexible solution for LunaNet constellations, which may include nodes that are not dedicated for PNT.

In this paper, we first formulated the equations of the dual one-way ISR measurements, and modeled how they are affected by the clock phase jumps. We then introduced two baseline methods to detect the clock phase jumps, based on the residuals of the ISR measurements, which are the sum of residuals method and the data snooping method.

Then, we proposed a new fault detection algorithm based on the EDMs and GCEDMs derived from the ISR measurements. We proved several properties of the rank of the EDM and GCEDM, as well as the distribution of the 4th singular value of the GCEDM. Based on these properties, we demonstrated that satellite fault can be detected by analyzing the 4th singular values of the GCEMs derived from ISR measurements. The proposed fault detection algorithm computes the sum of the GCEDM's 4th singular value for 5-clique subgraphs, and compares it to a threshold based on the chi-squared distribution of the 4th singular value under the presence of noise.

Through simulations of a GPS constellation and a notional lunar constellation, we compared the performance of the proposed method with the two baseline methods based on range residuals: the “sum of residuals” method and the “data snooping” method. The sum of residuals method performed well for larger fault magnitudes, but its detection power (TPR) was lower than the other two methods for smaller fault magnitudes. The data snooping method performed best among all methods when all ISRs containing fault satellites were corrupted, but its performance degraded when the biases were less observable (lunar scenario), and only a few ISRs were corrupted (e.g., due to link scheduling). The proposed EDM-based approach demonstrated balanced performance across different fault magnitudes and fault ratios for both GPS and lunar constellation scenarios.

This research marks a step towards establishing reliable PNT services for LunaNet. Future work will focus on link scheduling to optimize the number of ISRs available for fault detection under a constrained number of links, selecting effective subgraphs to reduce computation, looking into distributed implementation, and combining the EDM-based fault detection with residual-based fault detection methods to further enhance the robustness of the algorithm.

## ACKNOWLEDGEMENTS

We acknowledge Derek Knowles for reviewing the paper. This material is based upon work supported by The Nakajima Foundation and the National Science Foundation under Grant No. DGE-1656518.

## REFERENCES

Alawieh, M., Hadashik, N., Franke, N., & Mutschler, C. (2016). Inter-satellite ranging in the low earth orbit. *2016 10th International Symposium on Communication Systems, Networks and Digital Signal Processing (CSNDSP)*, 1–6. <https://doi.org/10.1109/CSNDSP.2016.7573920>

Alireza Motavallian, S., Yu, C., & Anderson, B. D. (2015). On the robustness to multiple agent losses in 2D and 3D formations: Multiple agent losses in 2d and 3d formations. *International Journal of Robust and Nonlinear Control*, 25(11), 1654–1687. <https://doi.org/10.1002/rnc.3167>

Baarda, W. (1968). A testing procedure for use in geodetic networks. *Netherlands geodetic commission*, 2(5).

Cao, Y., Hu, X., Chen, J., Bian, L., Wang, W., Li, R., Wang, X., Rao, Y., Meng, X., & Wu, B. (2019). Initial analysis of the BDS satellite autonomous integrity monitoring capability. *GPS Solutions*, 23, 35. <https://doi.org/10.1007/s10291-019-0829-z>

Chen, L., Dai, Y., Gao, W., Cao, Y., Hu, Z., Ren, Q., Nie, X., Zheng, J., Shao, R., Pei, L., & Wang, L. (2022). Performance analysis of bds-3 saim and enhancement research on autonomous satellite ephemeris monitoring. *Remote Sensing*, 14(15), 3543. <https://doi.org/10.3390/rs14153543>

Chiba, N., & Nishizeki, T. (1985). Arboricity and subgraph listing algorithms. *SIAM Journal on Computing*, 14(1), 210–223. <https://doi.org/10.1137/0214017>

de Jong, K., & Teunissen, P. J. G. (2014). Minimal detectable biases of gps observations for a weighted ionosphere. *Earth, Planets and Space*, 52(10), 857–862. <https://doi.org/10.1186/BF03352295>

Dokmanić, I., Parhizkar, R., Ranieri, J., & Vetterli, M. (2015). Euclidean distance matrices: Essential theory, algorithms and applications. *arXiv*. <https://doi.org/10.48550/arXiv.1502.07541>

Giordano, P., Swinden, R., Gramling, C., Crenshaw, J., & Ventura-Traveset, J. (2023). Lunanet position, navigation, and timing services and signals, enabling the future of lunar exploration. *Proceedings of the 36th International Technical Meeting of the Satellite Division of The Institute of Navigation (ION GNSS+ 2023)*, 3577–3588. <https://doi.org/10.33012/2023.19345>

Hendrickson, B. (1992). Conditions for unique graph realizations. *SIAM Journal on Computing*, 21(1), 65–84. <https://doi.org/10.1137/0221008>

Iiyama, K., Neamati, D., & Gao, G. (2024). Autonomous constellation fault monitoring with inter-satellite links: A rigidity-based approach. *Proceedings of the Institute of Navigation GNSS+ conference (ION GNSS+ 2024)*. <https://doi.org/10.33012/2024.19935>

Iiyama, K., Vila, G. C., & Gao, G. (2024). Contact plan optimization and distributed state estimation for delay tolerant satellite networks, 1–13. <https://doi.org/10.1109/AERO58975.2024.10521114>

Imhof, J. P. (1961). Computing the distribution of quadratic forms in normal variables. *Biometrika*, 48(3–4), 419–426. <https://doi.org/10.1093/biomet/48.3-4.419>

Imparato, D., Teunissen, P. J. G., & Tiberius, C. C. J. M. (2018). Minimal detectable and identifiable biases for quality control. *Survey Review*, 51(367), 289–299. <https://doi.org/10.1080/00396265.2018.1437947>

Israel, D. J., Mauldin, K. D., Roberts, C. J., Mitchell, J. W., Pulkkinen, A. A., Cooper, L. V. D., Johnson, M. A., Christe, S. D., & Gramling, C. J. (2020). LunaNet: A flexible and extensible lunar exploration communications and navigation infrastructure. *2020 IEEE Aerospace Conference*, 1–14. <https://doi.org/10.1109/AERO47225.2020.9172509>

Jian, L., Yang, Z., & Liu, Y. (2010). Beyond triangle inequality: Sifting noisy and outlier distance measurements for localization. *2010 Proceedings IEEE INFOCOM*, 1–9. <https://doi.org/10.1109/INFCOM.2010.5462019>

Knowles, D., & Gao, G. (2023). Euclidean distance matrix-based rapid fault detection and exclusion. *NAVIGATION: Journal of the Institute of Navigation*, 70(1). <https://doi.org/10.33012/navi.555>

Laman, G. (1970). On graphs and rigidity of plane skeletal structures. *Journal of Engineering Mathematics*, 4(4), 331–340. <https://doi.org/10.1007/BF01534980>

Lehmann, R., & Voß-Böhme, A. (2017). On the statistical power of baarda's outlier test and some alternative. *Journal of Geodetic Science*, 7(1), 68–78. <https://doi.org/10.1515/jogs-2017-0008>

Li, R., Gao, S., Qin, L., Wang, G., Yang, W., & Yu, J. X. (2020). Ordering heuristics for k-clique listing. *Proceedings of the VLDB Endowment*, 13, 2536–2548. <https://doi.org/10.14778/3407790.340784>

Misra, P., Bayliss, E., Lafrey, R., Pratt, M., & Muchnik, R. (1993). Receiver autonomous integrity monitoring (RAIM) of GPS and GLONASS. *NAVIGATION*, 40(1), 87–104. <https://doi.org/10.1002/j.2161-4296.1993.tb02296.x>

National Aeronautics and Space Administration. (2022). Lunar communications relay and navigation systems (LCRNS) preliminary lunar relay services requirements document (SRD). <https://esc.gsfc.nasa.gov/static-files/ESC-LCRNS-REQ-0090%20Rev.B%202012-05-2022%20DCN001.pdf>

Rathje, P., & Landsiedel, O. (2024). Time difference of arrival extraction from two-way ranging. *arXiv*. <https://doi.org/10.48550/arXiv.2204.08996>

Rodríguez-Pérez, I., García-Serrano, C., Catalán Catalán, C., García, A. M., Tavella, P., Galleani, L., & Amarillo, F. (2011). Inter-satellite links for satellite autonomous integrity monitoring. *Advances in Space Research*, 47(2), 197–212. <https://doi.org/10.1016/j.asr.2010.07.019>

Sitarz, M. (2023). Extending F1 metric, probabilistic approach. *Advances in Artificial Intelligence and Machine Learning*, 03(02), 1025–1038. <https://doi.org/10.54364/aaaiml.2023.1161>

Van Diggelen, F. S. T. (2009). *A-GPS: Assisted GPS, GNSS, and SBAS*. Artech house.

Walter, T., Gunning, K., Eric Phelts, R., & Blanch, J. (2018). Validation of the unfaulted error bounds for ARAIM. *NAVIGATION*, 65(1), 117–133. <https://doi.org/10.1002/navi.214>

Weiss, M., Shome, P., & Beard, R. (2010). On-board gps clock monitoring for signal integrity. *Proceedings of the 42nd Annual Precise Time and Time Interval Systems and Applications Meeting*, 465–480.

Wolf, R. (2000). Onboard autonomous integrity monitoring using intersatellite links. *Proceedings of the 13th International Technical Meeting of the Satellite Division of The Institute of Navigation (ION GPS 2000)*.

Xie, X., Geng, T., Ma, Z., Chen, L., & Liu, J. (2022). Estimation and analysis of bds-3 satellite yaw attitude using inter-satellite link observations. *GPS Solutions*, 26, 106. <https://doi.org/10.1007/s10291-022-01290-8>

Xu, H., Wang, J., & Zhan, X. (2011). Gnss satellite autonomous integrity monitoring (saim) using inter-satellite measurements. *Advances in Space Research*, 47(7), 1116–1126. <https://doi.org/10.1016/j.asr.2010.11.026>

Zhang, C., Geng, T., Xie, X., Zhao, Q., Li, T., Li, Z., & Meng, Y. (2024). Analysis of bds inter-satellite link ranging performance. *Advances in Space Research*, 73(10), 4955–4966. <https://doi.org/10.1016/j.asr.2024.02.023>

## A | COMPUTING THE TEST THRESHOLD USING IMHOF'S METHOD

In this section, we describe the procedure to obtain the critical value for the hypothesis test in section 3.1. The correlation between the two residuals that share the same satellites can be described as (Xu et al., 2011)

$$\rho(g_{i,j}, g_{i,k}) = \frac{\text{cov}(g_{i,j}, g_{i,k})}{\sqrt{\text{cov}(g_{i,j}, g_{i,j}) \cdot \text{cov}(g_{i,k}, g_{i,k})}} = \frac{\beta\sigma_r^2}{2\sigma_r^2 + \sigma_m^2} \quad (63)$$

where  $\beta$  is the cosine of the angle between two line-of-sight vectors  $e_{i,j}, e_{i,k}$ , that satisfies

$$\cos(\phi_{max}) < \cos(\beta) < \cos(0) = 1 \quad (64)$$

The covariance matrix  $\Sigma$  of the  $l_i$  normalized residuals  $\tilde{g}_{i,j} = g_{i,j} / \sqrt{2\sigma_r^2 + \sigma_m^2}$  obtained at satellite  $i$  can be described as

$$\Sigma_{i,j} = \begin{cases} 1 & i = j \\ \frac{\beta\sigma_r^2}{2\sigma_r^2 + \sigma_m^2} & i \neq j \end{cases} \quad (65)$$

Using the Imhof's method, the cumulative distribution function (CDF) value of the test statistic  $T_i = \sum_{j=1}^{l_i} \tilde{g}_{i,j}^2$  is given as (Imhof, 1961)

$$F_{\Sigma}(q) = P(T_i \leq q) = \frac{1}{2} - \frac{1}{\pi} \int_0^{\infty} \Im\left(e^{-itq} \cdot \phi(t)\right) \frac{dt}{t} \quad (66)$$

where  $\Im(\cdot)$  denotes the imaginary part, and the characteristic function  $\phi(t)$  is defined as

$$\phi(t) = - \prod_{k=1}^{l_i} \sqrt{1 - 2it\lambda_k} \quad (67)$$

where  $\lambda_k (k = 1, \dots, l_i)$  are the eigenvalues of the covariance matrix  $\Sigma$ . However, it is computationally expensive to evaluate equation (66) at every satellite at every timestep. Therefore, Xu et al. (2011) suggests to use the conservative bound for the cross-terms of  $\Sigma_{i,j}$ , as follows

$$\tilde{\Sigma}_{i,j} = \begin{cases} 1 & i = j \\ \frac{\sigma_r^2}{2\sigma_r^2 + \sigma_m^2} & i \neq j \end{cases} \quad (68)$$

Then, we can pre-compute  $F_{\tilde{\Sigma}}(q)$  for  $l_i = 1, \dots, N_s$ , and a pre-determined false alarm rate  $\alpha = 1 - q$ , and store them in a table. The test procedure using this conservative bound is

$$\text{Accept } \mathcal{H}_0 \text{ if } \max_{j \in \{1, \dots, n\}} T_i < F_{\tilde{\Sigma}}(1 - \alpha) \quad (69)$$

otherwise

$$\text{Accept } \mathcal{H}_k \text{ where } k = \operatorname{argmax}_{j \in \{1, \dots, n\}} \frac{T_j}{\sqrt{l_j}} \quad (70)$$

## B | PROOF OF PROPOSITION 4.1

*Proof.* Let  $r_{uv}$  be the observed inter-node distances. Consider a  $k$ -vertex redundantly rigid graph  $G$  with weight  $W(e_{uv}) = r_{uv}$  that is  $d$ -embeddable. Let  $\mathbf{q}: V \in \mathbb{R}^3$  be a generic realization (i.e, it does not lie on a plane or line, unless forced by the ranges) of the points with true inter-node distances  $\bar{r}_{uv}$  given by

$$\bar{r}_{uv} = \|\mathbf{q}_u - \mathbf{q}_v\| \quad (71)$$

and  $p: V \in \mathbb{R}^3$  be the generic realization of the points with the observed inter-node distances  $r_{uv}$

$$r_{uv} = \|\mathbf{p}_u - \mathbf{p}_v\| = \|\mathbf{q}_u - \mathbf{q}_v\| + f_{uv} \quad (72)$$

where  $f_{uv} \neq 0$  if  $u$  or  $v$  is the faulty satellite, and  $f_{uv} = 0$  otherwise.

Assume the following statement:

$$G \text{ contains } m \ (1 \leq m \leq k-1) \text{ faulty nodes} \quad (73)$$

Without the loss of generality, we can assume the indices of the faulty nodes are  $1, \dots, m$  for  $m \leq k-1$ . Let  $G' = G \setminus \{1, \dots, m\}$  a graph without the  $m \leq k-1$  faulty nodes. Since  $G$  is  $k$  vertex redundantly rigid,  $G'$  is rigid in  $\mathbb{R}^d$ . In addition, since  $G'$  contains no fault nodes, we have

$$\bar{r}_{uv} = r_{uv}, \quad u, v \neq \{1, \dots, m\} \quad (74)$$

Therefore, we may choose coordinates so that

$$\mathbf{p}_j = \mathbf{q}_j \quad j \neq \{1, \dots, m\} \quad (75)$$

For each fault node  $i \in \{1, \dots, m\}$ , its neighbor  $j \in \mathcal{N}(i)$ ,  $\mathcal{N}(i) = \{k | (i, k) \in G'\}$  satisfies

$$\|\mathbf{p}_u - \mathbf{p}_v\| = \|\mathbf{q}_i - \mathbf{q}_j\| + f_{ij} \quad (f_{ij} \neq 0) \quad (76)$$

Hence,  $\mathbf{p}_i$  must lie in the intersection

$$\bigcap_{j \in \mathcal{N}(i)} \left\{ x \in \mathbb{R}^3 : \|x - q_j\| = \|q_i - q_j\| + f_{ij} \right\}. \quad (77)$$

Geometrically, this is the common intersection of  $\|\mathcal{N}(i)\|$  spheres in  $\mathbb{R}^3$ . It is known that every vertex in a  $k$ -vertex redundantly rigid graph must have degree at least  $d+k-1$  (**Jordan2022extremal**). Since  $m \leq k-1$ , each fault node has at maximum  $k-2$  edges with other fault nodes (which are not included in  $G'$ ), and therefore we have  $\|\mathcal{N}(i)\| \geq (d+k-1) - (k-2) = 3-1+2 = 4$ .

Let  $\{j_1, \dots, j_4\} \in \mathcal{N}(i)$ , and

$$\mathbf{r} = [\|q_i - q_{j_1}\| + f_{ij_1} \quad \dots \quad \|q_i - q_{j_4}\| + f_{ij_4}]^\top \in \mathbb{R}^4 \quad (78)$$

Define a smooth map

$$F : \mathbb{R}^3 \longrightarrow \mathbb{R}^4 \quad F(x) = [\|x - q_{i_1}\| \quad \dots \quad \|x - q_{i_4}\|] \quad (79)$$

The spheres intersect if and only if

$$\mathbf{r} \in F(\mathbb{R}^3) \quad (80)$$

Since the Jacobian of  $F$  can have rank at most 3, its image  $F(\mathbb{R}^3) \subset \mathbb{R}^4$  is at most a 3-dimensional immersed submanifold of  $\mathbb{R}^4$ . Any smooth embedding of a  $k$ -dimensional manifold into  $\mathbb{R}^n$  has  $n$ -dimensional Lebesgue measure 0 whenever  $k < n$  (**GuilleminPollack1974**), and since the law of random radii vector  $\mathbf{r}$  is assumed continuous with respect to 4-dimensional Lebesgue measure, the probability that equation (80) is satisfied is 0. This contradicts the statement that the graph  $G$  is  $d$ -embeddable with the observed ranges, at probability 1. Since we derived a falsehood, the assumption (73) that the graph contains  $1 \leq m \leq k-1$  fault nodes is false, at probability 1. Therefore, if the graph is  $k$ -vertex rigid and is  $d$ -embeddable, and the graph contains at most  $k-1$  faulty nodes, the graph does not contain any fault nodes, at probability 1.  $\square$

## C | PROOF OF PROPOSITION 4.3

*Proof.* As discussed in Dokmanić et al. (2015), the noiseless- and faultless-EDM,  $\mathbf{D}_{ij}^{n,d,0} = \|\mathbf{x}_i - \mathbf{x}_j\|^2$ , based on a collection of points  $\mathbf{X} \in \mathbb{R}^{d \times n}$  can be constructed with Equation (81).

$$\mathbf{D}^{n,d,0} = \mathbf{1} \operatorname{diag}(\mathbf{X}^\top \mathbf{X})^\top - 2\mathbf{X}^\top \mathbf{X} + \operatorname{diag}(\mathbf{X}^\top \mathbf{X})\mathbf{1}^\top \quad (81)$$

where  $\operatorname{diag}(\mathbf{X}^\top \mathbf{X}) \in \mathbb{R}^n$  is the vector formed from the diagonal entries of  $\mathbf{X}^\top \mathbf{X}$ . The first and last matrices of Equation (81) are rank 1 matrices by construction. These rank 1 matrix each contribute to the matrix rank except for degenerate cases where the points are equally spread apart ( $\mathbf{X}\mathbf{1} = \mathbf{0}$ ). The middle term includes the Gram matrix  $\mathbf{X}^\top \mathbf{X}$ , which is rank  $d$  except for degenerate cases where the points lie on a lower dimensional hyperplane (i.e.,  $\operatorname{rank}(\mathbf{X}^\top \mathbf{X}) = 2$  if the points lie on a plane). So, in line with Dokmanić et al., 2015,  $\operatorname{rank}(\mathbf{D}^{n,d,0}) \leq d+2$ , where the condition holds with equality outside of the aforementioned degenerate cases.

During a fault, we encounter cross terms with the bias following Equation (82).

$$\begin{aligned}
 \mathbf{D}_{ij}^{n,d,m} &= (\|\mathbf{x}_i - \mathbf{x}_j\| + f_{ij})^2 = \|\mathbf{x}_i - \mathbf{x}_j\|^2 + 2\|\mathbf{x}_i - \mathbf{x}_j\|f_{ij} + f_{ij}^2 \\
 &= \|\mathbf{x}_i - \mathbf{x}_j\|^2 + f_{ij}(2\|\mathbf{x}_i - \mathbf{x}_j\| + f_{ij}) \\
 &= \|\mathbf{x}_i - \mathbf{x}_j\|^2 + f_{ij}(s_{ij} + f_{ij})
 \end{aligned} \tag{82}$$

Where  $s_{ij}$  is two times the elementwise square root of the corresponding entry in the EDM. As a matrix, we can write  $\mathbf{S}_{ij}^{n,d} = s_{ij}$ . We can write the bias term  $\mathbf{F}_{ij}^{n,m} = b_{ij}$  as a matrix as well. Both  $\mathbf{S}^{n,d}$  and  $\mathbf{F}^{n,m}$  are real, symmetric matrices. Then, we arrive at Equation (83).

$$\mathbf{D}^{n,d,m} = \mathbf{D}^{n,d,0} + \mathbf{F}^{n,m} \circ (\mathbf{S}^{n,d} + \mathbf{F}^{n,m}) \tag{83}$$

where  $\circ$  is the element-wise or Hadamard product. For the sake of illustration, consider the case with three faults of equal magnitude and opposite signs realized at satellites  $k = \{2, 3, 4\}$  for  $n > 7$ , without loss of generality.

$$\mathbf{F}^{n,\{2,3,4\}} = \bar{f} \begin{bmatrix} 0 & 1 & 1 & 1 & 0 & \cdots & 0 \\ 1 & 0 & 2 & 2 & 1 & \cdots & 1 \\ 1 & 2 & 0 & 2 & 1 & \cdots & 1 \\ 1 & 2 & 2 & 0 & 1 & \cdots & 1 \\ 0 & 1 & 1 & 1 & 0 & \cdots & 0 \\ \vdots & \vdots & \vdots & \vdots & \vdots & \ddots & \vdots \\ 0 & 1 & 1 & 1 & 0 & \cdots & 0 \end{bmatrix} = \bar{f} \begin{bmatrix} 0 & 1 & 1 & 1 \\ 1 & 0 & 2 & 2 \\ 1 & 2 & 0 & 2 \\ 1 & 2 & 2 & 0 \\ 0 & 1 & 1 & 1 \\ \vdots & \vdots & \vdots & \vdots \\ 0 & 1 & 1 & 1 \end{bmatrix} \begin{bmatrix} 1 & 0 & 0 & 0 & 1 & \cdots & 1 \\ 0 & 1 & 0 & 0 & 0 & \cdots & 0 \\ 0 & 0 & 1 & 0 & 0 & \cdots & 0 \\ 0 & 0 & 0 & 1 & 0 & \cdots & 0 \end{bmatrix} \tag{84}$$

In the rank-decomposition of  $\mathbf{F}^{n,m}$ , the column matrix has the first column has a one in each fault entry and a zero otherwise. This column spans all the  $n - m$  fault-free columns. The remaining  $m$  columns correspond to the columns in  $\mathbf{F}^{n,m}$  with faults and have a zero at the fault entry. In the example above, the entry 2 is illustrative. In general, the entry will depend on the fault magnitudes, which may be different. With probability zero, the faults across satellites exactly cancel out and lead to degeneracy in the fault detection, as discussed below.  $\mathbf{F}^{n,m}$  achieves full rank when the number of faults reaches  $m = n - 1$ . In general,  $\text{rank}(\mathbf{F}^{n,m}) = \min(1 + m, n)$  if  $m > 0$  and  $\text{rank}(\mathbf{F}^{n,0}) = 0$ . By similar argument,  $\text{rank}(\mathbf{F}^{n,m} \circ \mathbf{F}^{n,m}) = \text{rank}(\mathbf{F}^{n,m})$  since we will have one column indicating the fault entries and  $m$  columns associated with the columns of  $\mathbf{F}^{n,m} \circ \mathbf{F}^{n,m}$  with faults, which are the same columns as  $\mathbf{F}^{n,m}$ . This overall rank relationship often holds even if the faults are of different non-zero magnitudes. However, if the faults cancel out, the rank will drop. For example, in the case above, if  $b_2 = 2\bar{f}$  and  $b_3 = b_4 = -\bar{f}$ , then  $\text{rank}(\mathbf{F}^{n,m}) = 3$ . Therefore,  $\text{rank}(\mathbf{F}^{n,m}) \leq \min(1 + m, n)$  for arbitrary fault sizes. Nevertheless, the term  $\text{rank}(\mathbf{F}^{n,m} \circ \mathbf{F}^{n,m})$  can still be  $\text{rank } m + 1$  even if  $\text{rank}(\mathbf{F}^{n,m}) < m + 1$  since the squaring can remove the linear cancellation.

However, the span of the columns of  $\mathbf{F}^{n,m} \circ \mathbf{S}^{n,d}$  will generally span the columns  $\mathbf{F}^{n,m} \circ \mathbf{F}^{n,m}$ . Again, for the sake of illustration, we extend the example above with faults at satellites  $k = \{2, 3, 4\}$  for  $n > 7$ , without loss of generality.

$$\begin{aligned}
 \mathbf{F}^{n,\{2,3,4\}} \circ \mathbf{S}^{n,d} &= \bar{f} \begin{bmatrix} 0 & s_{12} & s_{13} & s_{14} & 0 & \cdots & 0 \\ s_{12} & 0 & 2s_{23} & 2s_{24} & s_{25} & \cdots & s_{2n} \\ s_{13} & 2s_{23} & 0 & 2s_{34} & s_{35} & \cdots & s_{3n} \\ s_{14} & 2s_{24} & 2s_{34} & 0 & s_{45} & \cdots & s_{4n} \\ 0 & s_{25} & s_{35} & s_{45} & 0 & \cdots & 0 \\ \vdots & \vdots & \vdots & \vdots & \vdots & \ddots & \vdots \\ 0 & s_{2n} & s_{3n} & s_{4n} & 0 & \cdots & 0 \end{bmatrix} \\
 &= \bar{f} \begin{bmatrix} 0 & s_{12} & s_{13} & s_{14} & 0 & 0 \\ s_{12} & 0 & 2s_{23} & 2s_{24} & s_{25} & s_{26} \\ s_{13} & 2s_{23} & 0 & 2s_{34} & s_{35} & s_{36} \\ s_{14} & 2s_{24} & 2s_{34} & 0 & s_{45} & s_{46} \\ 0 & s_{25} & s_{35} & s_{45} & 0 & 0 \\ \vdots & \vdots & \vdots & \vdots & \vdots & \vdots \\ 0 & s_{2n} & s_{3n} & s_{4n} & 0 & 0 \end{bmatrix} \begin{bmatrix} 1 & 0 & 0 & 0 & 0 & 0 & \Delta_{17} & \cdots & \Delta_{1n} \\ 0 & 1 & 0 & 0 & 0 & 0 & 0 & \cdots & 0 \\ 0 & 0 & 1 & 0 & 0 & 0 & 0 & \cdots & 0 \\ 0 & 0 & 0 & 1 & 0 & 0 & 0 & \cdots & 0 \\ 0 & 0 & 0 & 0 & 1 & 0 & \Delta_{57} & \cdots & \Delta_{5n} \\ 0 & 0 & 0 & 0 & 0 & 1 & \Delta_{67} & \cdots & \Delta_{6n} \end{bmatrix} \tag{85}
 \end{aligned}$$

where  $\Delta_{ij}$  are leftover terms from the row-reduction. In the rank-decomposition of  $\mathbf{F}^{n,m} \circ \mathbf{S}^{n,d}$ ,  $m$  columns correspond to the columns in  $\mathbf{F}^{n,m}$  with faults and have a zero at the fault entry, just as before. However, now, one column is generally not

enough to span the fault-free columns since the entries in  $\mathbf{S}^{n,d}$  are not linearly related. For example,  $(s_{12}, s_{13}, s_{14})$  is generally not a linear scaling of  $(s_{25}, s_{35}, s_{45})$ . These fault-free columns constitute an  $m$  dimensional subspace, from which will need  $m$  columns to fully span.  $\mathbf{F}^{n,m} \circ \mathbf{S}^{n,d}$  achieves full rank when the number of faults reaches  $m = \lceil n/2 \rceil$ , where  $\lceil \cdot \rceil$  is the ceiling function. At that point, the subspace of fault-free columns is large enough that the fault columns will contribute to the span. Therefore,  $\text{rank}(\mathbf{F}^{n,m} \circ \mathbf{S}^{n,d}) \leq \min(2m, n)$  where we do not have equality when  $\mathbf{S}^{n,d}$  is degenerate (i.e., if the fault satellites are above or below a plane of fault-free satellites).

The columns needed to span  $\mathbf{F}^{n,m} \circ \mathbf{S}^{n,d}$  are the same as those needed for  $\mathbf{F}^{n,m} \circ \mathbf{F}^{n,m}$ , with the same sparsity pattern. Therefore, we will have

$$\text{rank}(\mathbf{F}^{n,m} \circ (\mathbf{S}^{n,d} + \mathbf{F}^{n,m})) = \text{rank}(\mathbf{F}^{n,m} \circ \mathbf{S}^{n,d}) \leq \min(2m, n) \quad (86)$$

Lastly, the subspace spanned with the fault contributions is distinct from the subspace spanned by the EDM. Therefore,

$$\text{rank}(\mathbf{D}^{n,d,m}) \leq \min(d + 2 + 2m, n) \quad (87)$$

where the equality holds in non-degenerate cases. □

## D | PROOF OF PROPOSITION 4.4

*Proof.* First, by rank inequality  $\text{rank}(AB) \leq \min(\text{rank}(A), \text{rank}(B))$  for arbitrary matrices  $A$  and  $B$ . The rank of the geometric centring matrix is  $\text{rank}(\mathbf{J}^n) = n - 1$ . So,  $\text{rank}(\mathbf{G}^{n,d,k}) \leq n - 1$ . However, this bound is too loose when there are few faults. Expanding the expression for geometric centering yields Equation (88).

$$\begin{aligned} \mathbf{G}^{n,d,m} &= -\frac{1}{2}\mathbf{J}^n \mathbf{D}^{n,d,m} \mathbf{J}^n \\ &= -\frac{1}{2}\mathbf{J}^n (\mathbf{D}^{n,d,0} + \mathbf{F}^{n,m} \circ (\mathbf{S}^{n,d} + \mathbf{F}^{n,m})) \mathbf{J}^n \\ &= -\frac{1}{2}\mathbf{J}^n (\mathbf{1} \text{diag}(\mathbf{X}^\top \mathbf{X})^\top - 2\mathbf{X}^\top \mathbf{X} + \text{diag}(\mathbf{X}^\top \mathbf{X})\mathbf{1}^\top) \mathbf{J}^n - \frac{1}{2}\mathbf{J}^n (\mathbf{F}^{n,m} \circ (\mathbf{S}^{n,d} + \mathbf{F}^{n,m})) \mathbf{J}^n \end{aligned} \quad (88)$$

First, geometric centering removes the two rank 1 matrices, as shown in Equations (89) and (90) (Dokmanić et al., 2015).

$$-\frac{1}{2}\mathbf{J}^n (\mathbf{1} \text{diag}(\mathbf{X}^\top \mathbf{X})^\top) \mathbf{J}^n = -\frac{1}{2}(\mathbf{1} \text{diag}(\mathbf{X}^\top \mathbf{X})^\top - \mathbf{1} \text{diag}(\mathbf{X}^\top \mathbf{X})^\top)(\mathbf{I}^n - \frac{1}{n}\mathbf{1}\mathbf{1}^\top) = 0 \quad (89)$$

$$-\frac{1}{2}\mathbf{J}^n (\text{diag}(\mathbf{X}^\top \mathbf{X})\mathbf{1}^\top) \mathbf{J}^n = -\frac{1}{2}(\mathbf{I}^n - \frac{1}{n}\mathbf{1}\mathbf{1}^\top)(\text{diag}(\mathbf{X}^\top \mathbf{X})\mathbf{1}^\top - \text{diag}(\mathbf{X}^\top \mathbf{X})\mathbf{1}^\top) = 0 \quad (90)$$

For the  $-2\mathbf{X}^\top \mathbf{X}$  term, notice that the mean of the points is  $\mu = \frac{1}{n}\mathbf{X}\mathbf{1} \in \mathbb{R}^d$ . Using this property yields Equation (91), which is a Gram matrix of the form  $\mathbf{X}_c^\top \mathbf{X}_c$  for the point matrix  $\mathbf{X}_c$  centered about the origin (Dokmanić et al., 2015). This shift will not change the rank, meaning  $\text{rank}(\mathbf{X}^\top \mathbf{X}) = \text{rank}(\mathbf{X}_c^\top \mathbf{X}_c)$ .

$$-\frac{1}{2}\mathbf{J}^n (-2\mathbf{X}^\top \mathbf{X}) \mathbf{J}^n = (\mathbf{X} - \mu\mathbf{1}^\top)^\top (\mathbf{X} - \mu\mathbf{1}^\top) = \mathbf{X}_c^\top \mathbf{X}_c \quad (91)$$

The remaining term is  $\frac{1}{2}\mathbf{J}^n (\mathbf{F}^{n,m} \circ (\mathbf{S}^{n,d} + \mathbf{F}^{n,m})) \mathbf{J}^n$ . By rank inequality,

$$\text{rank}(\mathbf{J}^n (\mathbf{F}^{n,m} \circ (\mathbf{S}^{n,d} + \mathbf{F}^{n,m})) \mathbf{J}^n) \leq \min(\text{rank}(\mathbf{F}^{n,m} \circ (\mathbf{S}^{n,d} + \mathbf{F}^{n,m})), \text{rank}(\mathbf{J}^n)) = \min(2m, n - 1) \quad (92)$$

So, we are left with

$$\text{rank}(\mathbf{G}^{n,d,k}) \leq \min(d + 2m, n - 1) \quad (93)$$

□

## E | PROOF OF COROLLARY 4.4.1

*Proof.* In terms of rank, the noise acts as many small faults on each satellite, with the same sparsity structure as  $\mathbf{F}^{n,m}$  in Proposition 4.3, almost surely with  $m = n$  since there is zero probability mass that the randomly sampled noise is exactly zero or exactly cancel out. Using Proposition 4.4,

$$\text{rank}(\tilde{\mathbf{G}}^{n,d,m}) = \text{rank}(\mathbf{G}^{n,d,n}) \leq \min(d + 2n, n - 1) = n - 1 \quad (94)$$

Therefore, succinctly,  $\text{rank}(\tilde{\mathbf{G}}^{n,d,m}) = n - 1$ , almost surely.  $\square$

## F | THE DERIVATION OF THE SCALE OF CHI-SQUARED DISTRIBUTION

Let  $\mathbf{D} \in \mathbb{R}^{5 \times 5}$  the distance matrix between the nodes where  $D_{ij} = \|\mathbf{x}_i - \mathbf{x}_j\|$ , and  $\mathbf{E} \in \mathbb{R}^{5 \times 5}$  the perturbation matrix (the noise matrix) where  $E_{ij} = \omega_{ij} \sim \mathcal{N}(0, \sigma_m^2)$ . The observed noisy distance matrix is  $\tilde{\mathbf{D}} = \mathbf{D} + \mathbf{E}$ . The EDM is  $\mathbf{D} \circ \mathbf{D}$ , where  $\circ$  is the Hadamard (element-wise) product. The observed (noisy) GCEDM is

$$\begin{aligned} \tilde{\mathbf{G}} &= -\frac{1}{2}\mathbf{J}^5(\tilde{\mathbf{D}} \circ \tilde{\mathbf{D}})\mathbf{J}^5 \\ &= -\frac{1}{2}\mathbf{J}^5[(\mathbf{D} \circ \mathbf{D}) + 2(\mathbf{D} \circ \mathbf{E}) + (\mathbf{E} \circ \mathbf{E})]\mathbf{J}^5 \\ &\approx \mathbf{G} + \Delta\mathbf{G} \quad (\because \mathbf{E} \ll \mathbf{D}) \end{aligned} \quad (95)$$

where  $\Delta\mathbf{G} = \mathbf{J}^5(\mathbf{D} \circ \mathbf{E})\mathbf{J}^5$ . Here,  $\mathbf{G}$  has rank 3, and  $\tilde{\mathbf{G}}$  has rank 4, as proved in Corollary 4.4.1. Therefore,  $\text{rank}(\Delta\mathbf{G}) \geq 4 - 3 = 1$ , by rank subadditivity. Denote the singular value decomposition of  $\mathbf{G}$  as

$$\mathbf{G} = \mathbf{U}\Sigma\mathbf{V}^\top = [\mathbf{U}_1 \mid \mathbf{U}_0] \begin{bmatrix} \Sigma_3 & \mathbf{0}_{3 \times 2} \\ \mathbf{0}_{2 \times 3} & \mathbf{0}_{2 \times 2} \end{bmatrix} [\mathbf{V}_1 \mid \mathbf{V}_0]^\top \quad (\mathbf{U}_1, \mathbf{V}_1 \in \mathbb{R}^{5 \times 3} \text{ and } \mathbf{U}_0, \mathbf{V}_0 \in \mathbb{R}^{5 \times 2}) \quad (96)$$

From the SVD of the perturbed matrix  $\tilde{\mathbf{G}} = \tilde{\mathbf{U}}\tilde{\Sigma}\tilde{\mathbf{V}}^\top$ , we obtain

$$\begin{aligned} \tilde{\Sigma} &= \tilde{\mathbf{U}}^\top \tilde{\mathbf{G}} \tilde{\mathbf{V}} \\ &= (\mathbf{U} + \Delta\mathbf{U})^\top (\mathbf{G} + \Delta\mathbf{G})(\mathbf{V} + \Delta\mathbf{V}) \\ &= \Sigma + \mathbf{U}^\top(\Delta\mathbf{G})\mathbf{V} + \mathbf{U}^\top\mathbf{G}(\Delta\mathbf{V}) + \Delta\mathbf{U}^\top\mathbf{G}\mathbf{V} + [(\Delta\mathbf{U})^\top\Delta\mathbf{G}\mathbf{V} + \mathbf{U}^\top\Delta\mathbf{G}\Delta\mathbf{V} + (\Delta\mathbf{U})^\top\Delta\mathbf{G}\Delta\mathbf{V}] \\ &\approx \Sigma + \mathbf{U}^\top(\Delta\mathbf{G})\mathbf{V} + \Sigma\mathbf{V}^\top(\Delta\mathbf{V}) + \Delta\mathbf{U}^\top\mathbf{U}\Sigma \quad (\because \text{2nd and 3rd order perturbation } \approx 0) \\ &= \begin{bmatrix} \Sigma_3 + \mathbf{U}_1^\top\Delta\mathbf{G}\mathbf{V}_1 + \Delta_{11} & \mathbf{U}_1^\top\Delta\mathbf{G}\mathbf{V}_0 + \Delta_{12} \\ \mathbf{U}_0^\top\Delta\mathbf{G}\mathbf{V}_1 + \Delta_{21} & \mathbf{U}_0^\top\Delta\mathbf{G}\mathbf{V}_0 \end{bmatrix} \quad (\Delta_{11}, \Delta_{12}, \Delta_{21} : \text{perturbation from } \Sigma\mathbf{V}^\top(\Delta\mathbf{V}) + \Delta\mathbf{U}^\top\mathbf{U}\Sigma) \\ &= \begin{bmatrix} \Sigma_3 + \mathbf{U}_1^\top\Delta\mathbf{G}\mathbf{V}_1 + \Delta_{11} & \mathbf{0}_{3 \times 2} \\ \mathbf{0}_{2 \times 3} & \mathbf{U}_0^\top\Delta\mathbf{G}\mathbf{V}_0 \end{bmatrix} \end{aligned} \quad (97)$$

$\mathbf{U}_0^\top\Delta\mathbf{G}\mathbf{V}_0$  has rank 1 since  $\tilde{\mathbf{G}}$  has rank 4. Thus, the 4th singular value of  $\tilde{\mathbf{G}}$  satisfies

$$\lambda_4^2 = \tilde{\Sigma}_{44}^2 = \|\mathbf{U}_0^\top\Delta\mathbf{G}\mathbf{V}_0\|_F^2 \quad (98)$$

Since

$$\mathbb{E}[\lambda_4] = \mathbb{E}\|\mathbf{U}_0^\top\Delta\mathbf{G}\mathbf{V}_0\|_F = \mathbb{E}\|\mathbf{U}_0^\top\mathbf{J}^5(\mathbf{D} \circ \mathbf{E})\mathbf{J}^5\mathbf{V}_0\|_F = 0 \quad (\because \mathbb{E}[E_{ij}] = 0), \quad (99)$$

the squared 4th singular value  $\lambda_4^2$  follows a scaled chi-squared distribution with degree of freedom = 1. The scale of the distribution is equivalent to its expectation of the mean value, which is

$$\begin{aligned} s &= \mathbb{E}[\|\mathbf{U}_0^\top\mathbf{J}^5(\mathbf{D} \circ \mathbf{E})\mathbf{J}^5\mathbf{V}_0\|_F^2] \\ &= \mathbb{E}[\|(\hat{\mathbf{U}}^\top(\mathbf{D} \circ \mathbf{E})\hat{\mathbf{V}})\|_F^2] \quad (\hat{\mathbf{U}} = \mathbf{J}^5\mathbf{U}_0, \hat{\mathbf{V}} = \mathbf{J}^5\mathbf{V}_0 \in \mathbb{R}^{5 \times 2}) \\ &= \sum_{a=1}^2 \sum_{b=1}^2 \left( \mathbb{E} \left[ \left( \sum_{i=1}^5 \sum_{j=1}^5 \hat{U}_{i,a} D_{ij} E_{ij} \hat{V}_{j,b} \right)^2 \right] \right) \end{aligned} \quad (100)$$

The distribution of the product of the two elements in the noise matrices can be represented as

$$\mathbb{E}[E_{ij}E_{kl}] = \begin{cases} \sigma_m^2 & \text{if } (i,j) = (k,l) \text{ or } (i,j) = (l,k) \\ 0 & \text{otherwise} \end{cases} \quad (101)$$

Therefore, the scale of the distribution is

$$\begin{aligned} s &= \sum_{a=1}^2 \sum_{b=1}^2 \left[ \sum_{i=1}^5 \sum_{j=1}^5 2\sigma_m^2 \left( D_{ij} \hat{U}_{i,a} \hat{V}_{j,b} \right)^2 \right] \\ &= 2 \sum_{i=1}^5 \sum_{j=1}^5 (\sigma_m \mathbf{D}_{ij})^2 \cdot \|\hat{\mathbf{U}}_{i,:}\|^2 \cdot \|\hat{\mathbf{V}}_{j,:}\|^2 \quad (\hat{\mathbf{U}} = \mathbf{J}^5 \mathbf{U}_0, \hat{\mathbf{V}} = \mathbf{J}^5 \mathbf{V}_0 \in \mathbb{R}^{5 \times 2}) \end{aligned} \quad (102)$$

In addition, by comparison of the right bottom element of equation (97), we get

$$\tilde{\mathbf{U}}_0^\top (\mathbf{G} + \Delta \mathbf{G}) \tilde{\mathbf{V}}_0 = \mathbf{U}_0^\top \Delta \mathbf{G} \mathbf{V}_0 \quad (103)$$

where  $\tilde{U}_0, \tilde{V}_0$  are the 4th and 5th columns of  $\tilde{U}, \tilde{V}$ . Therefore, by plugging equation (98) into (103), we obtain the same scale as equation (102) by replacing  $D$  and  $U_0, V_0$  with the perturbed distance matrix  $\tilde{D}$  and singular vectors  $\tilde{U}_0, \tilde{V}_0$ . Therefore, we obtain

$$s = 2 \sum_{i=1}^5 \sum_{j=1}^5 (\sigma_m \tilde{\mathbf{D}}_{ij})^2 \cdot \|\hat{\mathbf{U}}_{i,:}\|^2 \cdot \|\hat{\mathbf{V}}_{j,:}\|^2 \quad (\hat{\mathbf{U}} = \mathbf{J}^5 \tilde{\mathbf{U}}_0, \hat{\mathbf{V}} = \mathbf{J}^5 \tilde{\mathbf{V}}_0 \in \mathbb{R}^{5 \times 2}) \quad (104)$$

## G | THE DERIVATION OF THE NON-CENTRALITY PARAMETER WHEN FAULT EXISTS

Let the fault satellite  $s_f$ , and all the ranges connected to the fault satellite is biased by  $\bar{f}$ . Using the same notation as Appendix F, the perturbed distance matrix  $\tilde{\mathbf{D}}_f$  is

$$\tilde{\mathbf{D}}_f = \mathbf{D} + \mathbf{F} + \mathbf{E} \quad (105)$$

where

$$\mathbf{F}_{ij} = \begin{cases} f_{ij} & i = s_f \text{ or } j = s_f \\ 0 & \text{otherwise} \end{cases} \quad (106)$$

Therefore, the perturbed GCEDM is

$$\tilde{\mathbf{G}}^f = -\frac{1}{2} \mathbf{J}^5 (\tilde{\mathbf{D}}_f \circ \tilde{\mathbf{D}}_f) \mathbf{J}^5 \approx \mathbf{G} + \Delta \mathbf{G}^f + \Delta \mathbf{G} \quad (107)$$

where

$$\Delta \mathbf{G}^f = \mathbf{J}^5 (\mathbf{F} \circ \mathbf{D}) \mathbf{J}^5 \quad (108)$$

From Colloary 4.4.1,  $\tilde{G}^f$  has rank 4. Following similar discussion as Appendix F, the 4th singular value of  $\tilde{G}^f$  satisfies

$$\lambda_4^2 = \Sigma_{44}^2 = \|\mathbf{U}_0^\top \Delta \mathbf{G} \mathbf{V}_0 + \mathbf{U}_0^\top \Delta \mathbf{G}^f \mathbf{V}_0\|_F^2 \quad (109)$$

The expectation of the singular value is

$$\begin{aligned} \mathbb{E}[\lambda_4] &= \mathbb{E}[\|\mathbf{U}_0^\top \Delta \mathbf{G} \mathbf{V}_0 + \mathbf{U}_0^\top \Delta \mathbf{G}^f \mathbf{V}_0\|_F] \\ &= \mathbb{E}[\|\mathbf{U}_0^\top \mathbf{J}^5 (\mathbf{D} \circ \mathbf{E}) \mathbf{J}^5 \mathbf{V}_0 + \mathbf{U}_0^\top \mathbf{J}^5 (\mathbf{D} \circ \mathbf{F}) \mathbf{J}^5 \mathbf{V}_0\|_F] \\ &> 0 \quad \left( \because \mathbb{E}[E_{ij}] = 0, \mathbb{E}[(D \circ F)_{ij}] = \begin{cases} D_{ij} f_{ij} \neq 0 & i = s_f \text{ or } j = s_f \\ 0 & \text{otherwise} \end{cases} \right) \end{aligned} \quad (110)$$

Therefore,  $\lambda_4^2$  follows the non-central chi-squared distribution. The expectation of the mean of the squared 4th singular value is

$$\begin{aligned}
 \mathbb{E}[\lambda_4^2] &= \mathbb{E} \left[ \|\mathbf{U}_0^T \Delta \mathbf{G} \mathbf{V}_0\|_F^2 \right] + \mathbb{E} \left[ \sum_{i=1}^2 \sum_{j=1}^2 (\mathbf{U}_0^T \Delta \mathbf{G} \mathbf{V}_0)_{ij} (\mathbf{U}_0^T \Delta \mathbf{G}^f \mathbf{V}_0)_{ij} \right] + \|\mathbf{U}_0^T \Delta \mathbf{G}^f \mathbf{V}_0\|_F^2 \\
 &= s + \|\mathbf{U}_0^T \Delta \mathbf{G}^f \mathbf{V}_0\|_F^2 \quad (\because \text{Eq. (100), } \mathbb{E}[(U_0^T \Delta G V_0)_{ij}] = 0) \\
 &= s \left( 1 + \frac{1}{s} \|\mathbf{U}_0^T \mathbf{J}(\mathbf{D} \circ \mathbf{F}) \mathbf{J} \mathbf{V}_0\|_F^2 \right)
 \end{aligned} \tag{111}$$

Therefore, the non-centrality parameter is given by

$$\lambda_{s_f} = \frac{1}{s} \|\mathbf{U}_0^T \mathbf{J}^5 (\mathbf{D} \circ \mathbf{F}) \mathbf{J}^5 \mathbf{V}_0\|_F^2 \tag{112}$$